Frictional and Hydraulic Properties of Plate Interfaces Constrained by a Tidal Response Model Considering Dilatancy/Compaction

Ryunosuke Sakamoto[1,1] and Yoshiyuki Tanaka[2,2]

[1]Osaka University
[2]University of Tokyo

November 30, 2022

Abstract

Tidal triggering of tectonic tremors has been observed at plate boundaries around the circum-Pacific region. It has been reported that the response of tremors to tidal stress during episodic tremor and slow slip (ETS) changes between the early and later stages of ETS. Several physical models have been constructed, with which observations for the tidal response during ETS have been partly reproduced. However, no model has been proposed that reproduces all the observations. In this study, a model adopted in previous studies is extended to include the effects of dilatancy/compaction that occur in the fault creep region. The analytical approximate solution derived in this study and numerical computational results reveal how the tidal response depends on the physical properties of the fault. Furthermore, the model reproduces all the above observations simultaneously for a specific range of fault parameters. Of particular importance is that the occurrence of dilatancy/compaction is essential to reproduce the tidal response at the early stage of the ETS. The value of the critical distance dc is constrained to be approximately 1~10 cm. This agrees with the values that have been widely used in seismic cycle numerical simulations rather than those obtained in laboratory experiments. The fluid pressure diffusivity is constrained to be at least 10^(-5) m^2/s or less, and the effective normal stress is constrained to 10^(5~6) Pa. In conclusion, this study shows that reproducing the tidal response of tectonic tremors during the ETS is useful for estimating fault physical properties, including hydraulic properties.

Frictional and Hydraulic Properties of Plate Interfaces Constrained by a Tidal Response Model Considering Dilatancy/Compaction

Ryunosuke Sakamoto[1] and Yoshiyuki Tanaka[2]

[1]Department of Earth and Space Science, Osaka University, Osaka, Japan

[2]Department of Earth and Planetary Science, University of Tokyo, Tokyo, Japan

Corresponding author: Ryunosuke Sakamoto (sakamoto@neq.ess.sci.osaka-u.ac.jp)

Key points:

- The spring-slider model with dilatancy/compaction reproduces the observed tidal response of tremors during episodic tremor and slip (ETS).
- The critical slip distance, diffusivity and effective stress are constrained by a comparison between the model and the observation.
- The pore fluid pressure change due to dilatancy/compaction is dominant at the early stage of the ETS, while it is negligible at the later stage.

Abstract

Tidal triggering of tectonic tremors has been observed at plate boundaries around the circum-Pacific region. It has been reported that the response of tremors to tidal stress during episodic tremor and slow slip (ETS) changes between the early and later stages of ETS. Several physical models have been constructed, with which observations for the tidal response during ETS have been partly reproduced. However, no model has been proposed that reproduces all the observations. In this study, a model adopted in previous studies is extended to include the effects of dilatancy/compaction that occur in the fault creep region. The analytical approximate solution derived in this study and numerical computational results reveal how the tidal response depends on the physical properties of the fault. Furthermore, the model reproduces all the above observations simultaneously for a specific range of fault parameters. Of particular importance is that the occurrence of dilatancy/compaction is essential to reproduce the tidal response at the early stage of the ETS. The value of the critical distance d_c is constrained to be approximately $1{\sim}10$ cm. This agrees with the values that have been widely used in seismic cycle numerical simulations rather than those obtained in laboratory experiments. The fluid pressure diffusivity is constrained to be at least $10^{-5}\ \mathrm{m^2/s}$ or less, and the effective normal stress is constrained to $10^{5\sim6}$ Pa. In conclusion, this study shows that reproducing the tidal response of tectonic tremors during the ETS is useful for estimating fault physical properties, including hydraulic properties.

Plain Language Summary

Slow earthquakes, which are slower fault slips than ordinary earthquakes, have been observed at many plate boundaries around the Pacific Rim. To understand how slow earthquakes occur, we need to know the exact physical fault properties that cause slow earthquakes. Previous studies have reported that the rate of occurrence of tectonic tremors, which are slow earthquakes, varies periodically in response to subsurface stress changes induced by tides. However, the detailed mechanism of the periodic behavior is still unclear. In this paper, we develop a theoretical model to explain this periodic behavior. A comparison between the observations in the Nankai Trough and Cascadia with our model shows that the pore fluid pressure in the vicinity of the fault changes significantly when tremors respond relatively weakly to tides. Furthermore, for the model to explain the observed tidal response of tremors, we find that the scale of the surface roughness of the fault should be much larger than those obtained by laboratory experiments and that the fault should have a low permeability.

1 Introduction

Recent geodetic and seismological observations have revealed that slow earthquakes occur in the transition zone, which is located at the deeper extension of the locked megathrust zone in a subduction zone. Slow earthquakes have various timescales, which are classified into low-frequency earthquakes (LFEs) with a major frequency of $2-8$ Hz (Obara, 2002), tectonic tremors, which are aggregations of LFEs (Shelly et al., 2007a), very low-frequency earthquakes (VLFEs) with a major frequency of $20-200$ Hz (Ito et al., 2007), and slow slip events (SSEs), which do not radiate seismic waves and continue to slip for more than a few days (Dragert et al., 2001; Hirose et al., 1999). The focal mechanism of these slow earthquakes indicates that they accommodate shear slip on the plate interface (e.g., Ide et al., 2007; Shelly et al., 2006). This focal mechanism coincides with that of ordinary earthquakes, which are caused by fast slip. It is well known that the fast slip behavior of an ordinary earthquake reflects the physical properties of the fault, which consist of friction, effective normal stress and dilatancy/compaction (e.g., Proctor et al., 2020; Scholz, 2019; Segall and Rice, 1995). The coincidence of the focal mechanism with those of slow earthquakes means that the slip behaviors of slow earthquakes should also reflect such fault physical properties. Therefore, it is important to clarify the physical fault properties in the transition zone to reveal the mechanism of slow earthquakes on various timescales.

In numerical simulation studies, several models have been proposed to reproduce slow earthquakes. These models usually adopt the rate- and state-dependent friction law (RSF) (e.g., Dieterich, 1979; Marone, 1998) as the frictional law on the plate interface. Examples of such models are those assuming near-neutral stability (e.g., Liu and Rice, 2005; Matsuzawa et al., 2010), dilatant strengthening of the shear zone (e.g., Liu, 2013; Segall et al., 2010), transition from velocity weakening (VW) at a low slip rate to velocity strengthening (VS) at a high slip rate (e.g., Im et al., 2020; Peng and Rubin, 2018; Shibazaki and Iio, 2003), spatial heterogeneity of frictional properties and effective normal stress (Luo and Ampuero, 2018), and sudden negative Coulomb stress change in the VS region due to fault valve action (Perfettini and Ampuro, 2008). Comparisons between such models and observed slow slip behaviors have allowed us to estimate the physical fault properties in the transition zone, which cannot be observed directly (e.g., Beeler et al., 2018; Luo and Liu, 2019; Nakata et al., 2012; Shibazaki et al., 2012).

In this study, we focus on tectonic tremors because they occur more frequently than other slow earthquakes, and it is easier to obtain more data to investigate the physical properties of faults. Tremors are classified into episodic families that accompany a SSE and continuous families that consist of tremors that occur almost daily (Thomas et al., 2018). The former is called episodic tremor and slip (ETS) (Obara et al., 2004; Rogers and Dragert, 2003). An important observation is that, for an ETS, there is a correlation between the slip rate of the SSE and the tremor occurrence rate (e.g., Bartlow et al., 2011; Hirose and Obara, 2010; Thomas et al., 2018; Villafuerte et al., 2017), even though the cumulative moment magnitude M_W of tremors is orders of magnitude smaller than that of SSEs (Kao et al., 2010). This correlation has been modeled by assuming that a tremor source is driven to failure by the stress loading due to aseismic slip that occurs in the region surrounding the tremor source (Shelly et al., 2007a). Based on this model, Shelly et al. (2011) interpreted the delayed dynamic triggering of tremors as a result of transient creep induced by the passage of seismic waves. Similarly, Tan and Marsan (2020) interpreted that the spatial anisotropy of the SSE during an ETS causes anisotropy in the power law describing a spatial decay of tremors.

Another important observational fact revealed by global observations of tremors is that tremors are sensitive to tidal stress (e.g., Chen et al., 2018; Hoston, 2015; Ide and Tanaka, 2014; Ide et al., 2015; Nakata, 2008; Royer et al., 2015; Rubinstein et al., 2008; Shelly et al., 2007b; Thomas et al., 2009, 2012; Van Der Elst et al., 2016; Yabe et al., 2015).

In general, stress changes on faults due to semidiurnal and diurnal tides are a few kPa or smaller. These stress changes are much smaller than the stress drop of ordinary earthquakes. Observational studies have reported that, in some cases, a weak correlation can be seen between earthquakes and tidal stresses (e.g., Cochran et al., 2004; Métivier et al., 2009; Tanaka 2010, 2012). The tidal response of earthquakes has also been studied by laboratory experiments using a stress perturbation to rock or granular materials (e.g., Bartlow et al., 2012; Beeler and Lockner 2003; Chanard et al., 2019; Lockner and Beeler, 1999; Noël and Passelègue et al., 2019; Noël and Pimienta et al., 2019; Savage and Marone, 2007). For example, the results of Chanard et al. (2019) and Noël and Pimienta et al. (2019) are consistent with the observation results of Tanaka (2010, 2012) regarding the tidal response that appears before a large earthquake. Other studies have reported that no correlation is seen between earthquakes and tidal stresses (e.g., Heaton 1982; Vidale et al., 1998; Wein and Shearer 2004).

The tidal response of tremors is clearer because the pore fluid pressure on the plate interfaces is much higher in the transition zone than in the seismogenic zone, and hence, the effective normal stress is extremely low (Audet et al., 2009; Shelly et al., 2006).

The tidal response of tremors can be characterized by a tidal sensitivity and a phase difference. The tidal sensitivity, α, characterizes the magnitude of tidal modulation of the tremor rate (i.e., the number of observed tremor events per unit time); the relationship between the tremor rate and the tidal Coulomb stress change is described by

$$R = R_0 e^{\alpha \Delta S(t)}, \tag{1}$$

where R denotes the tremor rate, $\Delta S(t)$ is the tidal Coulomb stress, and R_0 is the reference tremor rate when $\Delta S(t) = 0$. In equation (1), the order of the tidal sensitivity is $0.01{\sim}1$ kPa^{-1} (e.g., Houston, 2015; Ide et al., 2015; Royer et al., 2015; Thomas et al., 2012; Yabe et al., 2015). The phase difference, defined as δ,, represents the phase shift between the tremor rate peak (i.e., the phase at which R is maximum) and the tidal stress peak (i.e., the phase at which $\Delta S(t)$ is maximized). δ is positive when the tremor rate reaches its maximum before the tidal stress reaches its maximus. For example, when the peak of R precedes the peak of $\Delta S(t)$ in the semidiurnal tide (approximately 12 hour cycle) by 3 hours, $\delta{\sim}\pi/2$. Previous studies have reported that α and δ change at the early and later stages of the ETS (Houston, 2015; Royer et al., 2015; Yabe et al., 2015). At the early stage of an ETS, $\alpha \lesssim 0.1$ kPa^{-1} (meaning that tidal modulation of the tremor rate is smaller) and $\delta{\sim}\pi/2$. At the later stage of the ETS, $\alpha{\sim}0.7$ kPa^{-1} (meaning that the tidal modulation of the tremor rate is larger) and $\delta{\sim}0$. In addition, the number of tremors occurring at the later stage of ETS is approximately $1/10$ or less than at the early stage of ETS (Houston, 2015; Royer et al., 2015).

Constructing a model that reproduces such observed tidal responses of tremors is an effective method to infer the physical properties of faults because tidal stress change, which serves as an “input” to a fault slip model to reproduce the tidal response, is much easier to estimate. Previous studies have proposed several models to interpret the observed tidal response of tremors (Ader et al., 2012; Beeler et al., 2013; Beeler et al., 2018; Hawthorne and Rubin, 2013; Houston, 2015). These models are classified into deterministic models that adopt the physical model proposed by Shelly et al. (2007a) and a stochastic model that adopts the Weibull distribution as the failure strength of tremor sources. Furthermore, deterministic models are classified into two models: one considers the change in the pore fluid pressure at the plate interface, and the other does not (Table 1).

Specifically, under the assumption that the tremor rate is proportional to fault creep velocity, Ader et al. (2012), Beeler et al. (2013) and Hawthorne and Rubin (2013) investigated the tidally modulated tremor rate. Ader et al. (2012) adopted the RSF for the VS to describe the tidal modulation of the fault creep velocity. They showed that the tidal sensitivity and the phase difference (the phase difference between the fault creep velocity peak and the tidal stress peak) depend on the tidal period, fault creep velocity and frictional properties. Based on this result, they provided a framework to explain the tidal sensitivity and the phase difference in terms of tidal period, fault creep velocity and frictional properties. Beeler et al. (2013) compared dislocation creep, dislocation glide and the RSF for the VS region to explain the exponential relationship of equation (1) and concluded that the exponential behavior was derived from the RSF for the VS region. Based on a model that follows the RSF assuming a transition from the VW at a lower slip velocity to the VS at a higher slip velocity, Hawthorne and Rubin (2013) showed that the tidal modulation of the fault creep velocity increases as the fault creep average velocity decreases. Based on a probabilistic model, Houston (2015) interpreted that the tidal response of tremors is different between the early stage and later stages of ETS due to a gradual decrease in the fault strength for the tremor sources. Beeler et al. (2018) reproduced the observed tidal response of tremors of the continuous families based on a model assuming the RSF of the VW and estimated fault physical properties of the transition zone, such as the fluid pressure diffusivity and dilatancy coefficient.

Table 1. A summary of previous models and our model

Paper that proposed the model	Model type	Introduction of fluid pressure change by dilatancy/compaction	Reproduction of tidal response of tremor at the early stage of ETS	Reproduction of tidal response of tremor at the later stage of ETS
Ader et al. (2012)	Deterministic	No	Tidal period $> 10^8$ s	Yes
Beeler et al. (2013)	Deterministic	No	Cannot reproduce phase difference	Yes
Hawthorne and Rubin (2013)	Deterministic	No	Cannot reproduce phase difference	Yes
Houston (2015)	Probabilistic	—	Yes[a]	Yes[a]
Beeler et al. (2018)	Deterministic	Yes	—[b]	—[b]
This study	Deterministic	Yes	Yes	Yes

[a] The model assumption may not be valid. [b] The model is not applicable to the tidal modulation of tremors during ETS.

Most of the above models only partially explain the observations of the tidal response of tremors during ETS with several advantages (Table 1). Ader et al. (2012) investigated the slip behavior of a one-degree-of-freedom spring-slider system under a harmonic stress perturbation with different periods. Their model could reproduce the tidal response of tremors at the later stage of the ETS when considering diurnal and semidiurnal tidal periods (~10^5 s). However, the model could not reproduce the phase difference of $\delta \sim \pi/2$ observed at the early stage of ETS unless adopting much longer tidal periods (e.g., 18.6 years tide) (>10^8 s). Beeler et al. (2013) and Hawthorne and Rubin (2013) modeled the tidal modulation of fault creep velocity using a purely rate-dependent friction law and a frictional law assuming a transition from the VW to VS region, respectively. Their results show that the fault creep velocity increases as the tidal stress increases. This suggests that these models could explain the tidal response of tremors at the later stage of the ETS but not the phase difference observed at the early stage of the ETS ($\delta \sim \pi/2$). The model of Houston (2015) assumes that breakage of mineral precipitates due to slip accumulation during the ETS might weaken the fault strength. This model may contradict the idea of dilatant strengthening, which assumes that fault strength increases with increasing pore space due to breakage of precipitating minerals (Audet and Bürgmann, 2014). Beeler et al. (2018) modeled the correlation between LFE clusters and tidal stress for continuous families. Their model focused only on the onset of the clusters. Therefore, their model cannot be applied to the tidal modulation of tremors that lasts for 1~2 weeks during ETS. Therefore, the models proposed thus far cannot fully explain the aspects of the observed tidal responses of tremors.

Here, we propose a new model in which dilatancy/compaction occurs in the VS region to explain the observed tidal response of tremors during the ETS. We find that the pore fluid pressure changes due to dilatancy/compaction caused by tidal stress change in the transition zone, where the effective normal stress is low, have a significant influence on the sliding behavior in the VS zone. We present governing equations for this problem in section 2. In the next section, we derive an approximate solution to quantitatively describe α and δ and clarify how the model responds to tidal stress changes. We reveal the physical reason for the dependence of α and δ on the fault physical properties. In section 4, we estimate fault physical properties based on a comparison between the observations and our model results and discuss the validity of the estimated properties. In section 5, we summarize the results.

2 Methods

2.1 Modeling the rate of tremor occurrence

Similar to previous studies, we assume that tremors are generated by the rupture of small brittle patches on the fault plane due to the aseismic shear slip of a larger-scale surrounding fault (Ader et al., 2012; Beeler et al., 2013; Shelly et al., 2007a). This assumption means that the tremor source is very small and that the tremor rate, R, serves as a passive meter of the creep velocity of the surrounding fault, V:

$$\frac{V}{V_r} = \frac{R}{R_r}, \tag{2}$$

where R_r and V_r denote the tremor rate and the creep velocity at a reference state, respectively. Based on this assumption, we can regard a change in the tremor rate as a change in the creep velocity. Equation (2) has been adopted in previous studies that modeled the tidal response of tremors and LFEs (e.g., Ader et al., 2012; Beeler et al., 2013).

2.2 Governing equations

2.2.1 Rate- and state-dependent friction law

We model the above fault creep, assuming a one-degree-of-freedom spring-slider system and employ the RSF as a friction law (Ader et al., 2012). According to the RSF, the friction coefficient μ can be written as:

$$\mu = \mu_0 + a\log\left(\frac{V}{V_0}\right) + b\log\left(\frac{V_0\theta}{d_c}\right), \tag{3}$$

where μ_0 denotes the friction coefficient at a reference slip velocity V_0, V is the slip velocity, d_c is the critical slip distance, θ is the state variable, which is often interpreted as the average contact time for an asperity, and a and b are fault constitutive parameters (e.g., Scholz, 1998). To represent fault creep, the constitutive parameters must satisfy $a > b$. This regime is called VS. In equation (3), the second term on the right-hand side (RHS) represents the "direct effect", which is caused by a change in the slip velocity, and the third term on the RHS represents the "evolution effect", which is caused by the temporal change in the state variable. Fault slip behavior evolves to a new steady state when a sudden slip velocity change occurs and the fault slips over a distance of d_c (Dieterich, 1979). This process can be expressed in several ways. In this study, we adopt the slip law proposed by Ruina (1983):

$$\frac{\mathrm{d}\theta}{\mathrm{d}t} = -\frac{V\theta}{d_c}\log\left(\frac{V\theta}{d_c}\right). \tag{4}$$

2.2.2 Dilatancy/Compaction

Dilatancy/compaction is a mechanism that relates fault gouge deformation to the behavior of the pore fluid. A shear zone exists at and near the plate interface where shear slip is localized and fault gouge is present (e.g., Rice, 2006). We assume that the porosity change in the shear zone is caused by dilatancy/compaction (e.g., Segall et al., 2010; Suzuki and Yamashita, 2009). The associated behavior of pore fluids can be modeled as in the following two cases. The first is an undrained model, which assumes that the pore fluid pressure changes only within the shear zone (Figure S1a in the supporting information), and the second is a drained model, which assumes a "homogeneous diffusion" of the pore fluid into a region adjacent to the shear zone (Segall et al., 2010) (Figure S1b in the supporting information). Since our model is a one-degree-of-freedom system, the pore fluid pressure is uniform in the direction of the slip plane, and the pore fluid pressure diffuses in the direction perpendicular to the slip plane. The pore fluid pressure in the shear zone is spatially uniform in both the drained and undrained models. Let a tidal period be T (e.g., 12.4 hours) and the characteristic timescale at which the pore fluid pressure diffuses through the shear zone be t_w. The undrained model is valid when $T \ll t_w$ (Beeler et al., 2018), and the drained model is valid when $T \gg t_w$ (Segall et al., 2010). As described later (section 4.2), the undrained model can explain the tidal response at the early and later stages of the ETS, while the drained model cannot explain the tidal response at the early stage of the ETS. We focused on the results for the undrained model in the main text, which can reproduce more observations than the drained model. The derivation of the governing equations and results for the drained model are shown in the supporting information (Texts S1-S4, Figures S3, S4 and S6).

Mathematically, in the undrained model, the pore fluid pressure change in the shear zone can be described as

$$\frac{\mathrm{d}p}{\mathrm{d}t} = -M\frac{\mathrm{d}\phi}{\mathrm{d}t}, \tag{5}$$

which is derived from the conservation of pore fluid mass (Segall et al., 1995), where $\mathrm{d}p/\mathrm{d}t$ denotes a temporal change in the pore fluid pressure, M is the bulk modulus of the fluid and the pore space, and $\mathrm{d}\phi/\mathrm{d}t$ denotes a change in the porosity due to dilatancy/compaction. As described previously, for the friction coefficient (equation (3)), the porosity, which varies with dilatancy/compaction, also evolves from one steady state to another as the slip velocity changes. The evolution law for the porosity can be empirically described as

$$\frac{\mathrm{d}\phi}{\mathrm{d}t} = -\frac{\epsilon}{\theta}\frac{\mathrm{d}\theta}{\mathrm{d}t}, \tag{6}$$

using the state variable θ, where ϵ is a dilatancy coefficient (Segall and Rice, 1995). From equations (5) and (6), we obtain

$$\frac{\mathrm{d}p}{\mathrm{d}t} = \epsilon M \frac{1}{\theta}\frac{\mathrm{d}\theta}{\mathrm{d}t} \ . \tag{7}$$

2.2.3 A quasi-static equation of motion

The quasi-static equation of motion for the one-degree-of-freedom spring-slider model under tidal stress can be written as

$$\Delta\tau(t) + k\Delta u = \mu\sigma_{eff}(t), \tag{8}$$

where $\Delta\tau(t)$ denotes the shear stress acting on the fault plane due to tides, $\sigma_{eff}(t)$ is the effective normal stress, Δu is the relative displacement of the block to the spring pulling distance, k is the spring stiffness and μ is the friction coefficient (Ader et al., 2012; Perfettini and Schmittbuhl, 2001). In our model, the effective normal stress is written as $\sigma_{eff}(t) = \sigma_{eff}^0 + \Delta\sigma(t) - \Delta p(t) - \Delta p'(t)$, where σ_{eff}^0 denotes a reference effective normal stress, $\Delta\sigma(t)$ is the normal stress acting on the fault plane due to tides, $\Delta p(t)$ is the pore fluid pressure change due to dilatancy/compaction in the shear zone, and $\Delta p'(t)$ is the pore fluid pressure change due to the tidal normal stress change. When the tidal normal stress increases, $\Delta p'(t)$ also increases in proportion to the Skempton coefficient, B (i.e., $\Delta p'(t) = B\Delta\sigma(t)$) (e.g., Beeler et al., 2018; Scholz et al., 2019). Using this relationship, the effective normal stress can be rewritten as

$$\sigma_{eff}(t) = \sigma_{eff}^0 + (1-B)\Delta\sigma(t) - \Delta p(t). \tag{9}$$

The observations show that there is almost no correlation between the tidal normal stress change and the tremor rate (Houston, 2015; Thomas et al., 2012), which indicates that the fault strength is almost unchanged due to the tidal normal stress change. This suggests that B is nearly equal to 1 (equation (9)). Therefore, we adopt $B = 0.9$ in our model. For simplicity, we assume that the tidal stresses $\Delta\sigma(t)$ and $\Delta\tau(t)$ have a common period with the same magnitude and phase (i.e., $\Delta\sigma(t) = \Delta\tau(t) = |\Delta\sigma(t)|e^{i\omega t}$).

2.3 Nondimensionalization of governing equations

Equations (3), (4), (7) and (8) constitute the governing equations for our model. For nondimensionalization of these equations, we selected a tidal period T, a reference effective normal stress σ_{eff}^{0}, and a critical slip distance d_c as characteristic physical quantities (Table 2). Representing the dimensionless variables with a tilde, the result is written as:

$$\mu = \mu_0 + a\log\left(\frac{\tilde{V}}{\tilde{V}_0}\right) + b\log\left(\frac{\tilde{\theta}}{\tilde{\theta}_0}\right)$$

$$\Delta\tilde{\tau} + \tilde{K}\Delta\tilde{u} = \mu\tilde{\sigma}_{eff}$$

$$\frac{\mathrm{d}\tilde{\theta}}{\mathrm{d}\tilde{t}} = -\tilde{\theta}\tilde{V}\log\left(\tilde{\theta}\tilde{V}\right)$$

$$\frac{\mathrm{d}\tilde{p}}{\mathrm{d}\tilde{t}} = \frac{U}{\tilde{\theta}}\frac{\mathrm{d}\tilde{\theta}}{\mathrm{d}\tilde{t}}, \qquad (10)$$

where $\theta_0 = d_c/V_0$ denotes the state variable at a reference slip velocity V_0, $\tilde{K} = d_c k/\sigma_{eff}^{0}$ is the nondimensional spring constant, and $U = M\epsilon/\sigma_{eff}^{0}$ is the dilatancy parameter. Substituting the last equation in equation (10) into the nondimensionalized version of equation (9), we find that the larger U is, the more dominant the effect of $\Delta p(t)$ on the effective normal stress is. In other words, the parameter U represents the relative importance of the dilatancy/compaction to the effective normal stress change. Previous experiments and observations suggest that $\sigma_{eff}^{0}{\sim}10^{5\sim6}$ Pa (Nakata et al., 2008; Shelly et al., 2006; Yabe et al., 2015), $\epsilon{\sim}10^{-4\sim-5}$ (Samuelson et al., 2009), and $M{\sim}10^{10}$ Pa (Segall et al., 1995). This yields a possible range of U from 10^{0} to 10^{-2}.

The time evolution of each physical quantity is numerically calculated using the fourth-order Runge–Kutta method.

Table 2. Parameters of fault physical properties

Parameter	Value
Reference velocity V_0	10^{-9} m/s
Spring pulling velocityV_{pl}	10^{-8} m/s
Reference frictional coefficient μ_0	0.7
Reference effective normal stress σ_{eff}^{0}	500 kPa

Skempton coefficient B	0.9
Spring stiffness k	10^4 Pa/m
Magnitude of tidal shear stress$\vert\Delta\tau(t)\vert$	1 kPa
Magnitude of tidal normal stress$\vert\Delta\sigma(t)\vert$	1 kPa
Tidal period T	12.4 h
Frictional parameter a	0.003
Frictional parameter b	0.002
Dilatancy parameter$U$	$10^{-2\sim 0}$

2.4 Definition of the tidal sensitivity (α) and the phase difference (δ)

In previous studies, α has been estimated using equation (1), and δ has been inferred using the phase difference between the tidal Coulomb stress peak and the tremor rate peak (Houston, 2015; Royer et al., 2015; Yabe et al., 2015); we define α and δ in the same way. In the following, we refer to these two parameters as the "tidal response".

To illustrate the definition of these two quantities and how to determine them, Figure 1 shows a result obtained by numerically solving the governing equations for the case of $U = 0$ and $d_c = 100$ μm. The solid yellow line in Figure 1a is the time evolution of $V(t)/V_{pl}$ during one tidal cycle. The solid yellow line in Figure 1b shows $V(t)/V_{pl}$ in Figure 1a against the tidal Coulomb stress change $\Delta S(t)$, and the solid green line shows the average of the upper and the lower values of $V(t)/V_{pl}$ at each $\Delta S(t)$ on the horizontal axis, where

$$\Delta S(t) = \Delta\tau(t) - \mu_{pl}(1 - B)\Delta\sigma(t) \tag{11}$$

(e.g., Beeler et al., 2018; Scholz et al., 2019), and μ_{pl} is the steady-state friction coefficient at velocity V_{pl}. The reason why $\Delta S(t)$ is described by $\Delta\tau(t) - \mu_{pl}(1 - B)\Delta\sigma(t)$ instead of $\Delta\tau(t) - \mu_{pl}\Delta\sigma(t)$ is that, for a poroelastic medium, the effective normal stress change due to tides is described by $(1 - B)\Delta\sigma(t)$ from equation (9). α is obtained by fitting the following equation to the average of $V(t)/V_{pl}$ (solid green line in Figure 1b):

$$\frac{V(t)}{V_{pl}} = ce^{\alpha\Delta S(t)}. \tag{12}$$

In the fitting, a constant $c(< 1)$ is simultaneously determined. If c is not estimated, the following problem arises. Since our model pulls the block through the spring with velocity V_{pl}, the block must slip with V_{pl} on a long-term average ($\int_0^T V(t)\,dt/T = V_{pl}$ with $T \gg 0$). Equation (12) shows $V(t) \propto e^{\Delta S(t)}$, indicating that the slip velocity increases nonlinearly with ΔS(t). If $V(t) = V_{pl}$ at $S(t) = 0$ (equivalently $c = 1$), it is unphysical because.$\int_0^T V(t)\,dt/T > V_{pl}$. Therefore, $V(t) < V_{pl}$ at $S(t) = 0$ (equivalently $c < 1$) is needed. The parameter c adjusts the average velocity but has nothing to do with the estimation of fault physical properties in the following. Figure S2 shows the obtained value of c. The solid black line in Figure 1b shows the fitted result. δ is defined as the phase difference between the $\Delta S(t)$ peak and the $V(t)/V_{pl}$ peak (see δ of Figure 1a), where δ is positive when the $V(t)/V_{pl}$ peak precedes the $\Delta S(t)$ peak (i.e., δ in Figure 1a is negative).

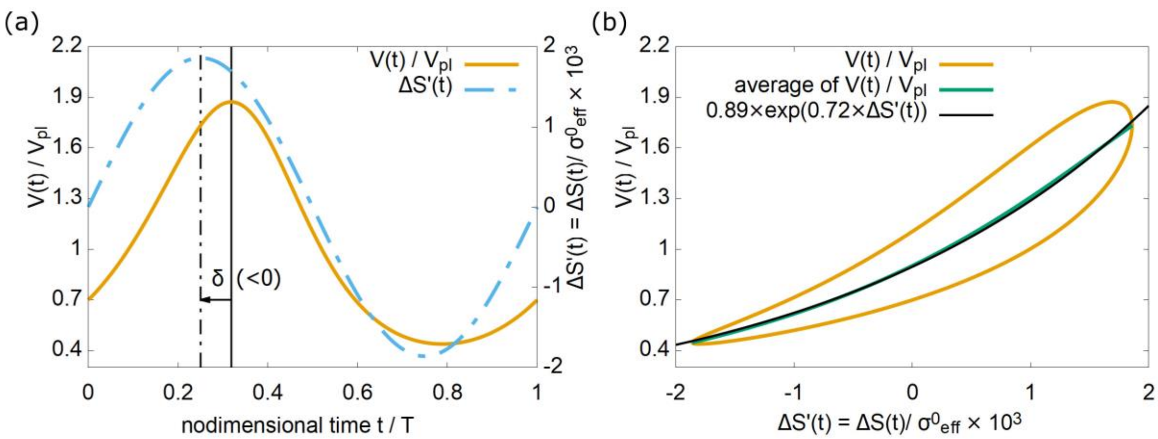

Figure 1. The numerical solution of equation (10) for $U = 0$ and $d_c = 100$ μm. (a) Determination of the phase difference (δ). The horizontal axis denotes time normalized by the tidal cycle, and the value from 0 to 1 indicates one tidal cycle. The vertical axis represents the slip velocity normalized by the reference velocity, $V(t)/V_{pl}$. The solid yellow line shows $V(t)/V_{pl}$, and the dashed blue line shows the tidal Coulomb stress, $\Delta S(t) \times 10^3$, normalized by the reference effective normal stress, σ_{eff}^0. The dashed black line represents the phase when $\Delta S(t)$ reaches the maximum, and the solid black line represents the $V(t)/V_{pl}$ peak. The phase difference δ is defined so that it is positive when the $V(t)/V_{pl}$ peak precedes the $\Delta S(t)$ peak. (b) Determination of the tidal sensitivity (α). The horizontal axis is $\Delta S'(t) = \Delta S(t)/\sigma_{eff}^0 \times 10^3$. The vertical axis represents the slip velocity normalized by the reference velocity, $V(t)/V_{pl}$. The solid yellow line shows $V(t)/V_{pl}$ in (a). The solid green line shows the average of

the upper and lower velocities at each value of $\Delta S'(t)$. c and α in equation (12) are determined by a least squares method by fitting equation (12) against the green solid line. The solid black line shows the fitted result ($\alpha = 0.72, c = 0.89$).

2.5 An approximate solution for α and δ

To clarify how the tidal responses depend on the fault physical properties, we analytically derived an approximate solution for α and δ. The result is shown in section 3.1.

3 Result

3.1 Derivation and verification of the approximate solution

When the magnitude of the tidal Coulomb stress change $|\Delta S(t)|$ is small enough ($|\Delta S(t)| \ll (a-b)\sigma_{eff}^0$), we assume that the perturbation of each physical quantity caused by $|\Delta S(t)|e^{i\omega t}$ is proportional to $e^{i\omega t}$, where $\omega = 2\pi/T$ is the angular velocity of the tide (Segall, 2010; Ader et al., 2012). In other words, the physical quantities can be written as $V(t) = V_{pl} + \Delta V e^{i\omega t}$, $\theta(t) = \theta_{pl} + \Delta\theta e^{i\omega t}$ and $p(t) = p_0 + \Delta p e^{i\omega t}$, where θ_{pl} denotes the steady-state variable at $V = V_{pl}$, p_0 is the reference value of pore fluid pressure, and ΔV, $\Delta\theta$ and Δp are the magnitudes of the perturbation. Substituting these forms into equations (3), (4), (7), and (8), and after some algebra, the perturbation of the nondimensionalized slip velocity, $\Delta\tilde{V}$, can be written as

$$\frac{\Delta\tilde{V}}{\tilde{V}_{pl}} = \frac{2\pi i}{\tilde{K}\tilde{V}_{pl} + 2\pi i A}|\Delta\tilde{S}(t)|, \qquad (13)$$

where

$$A = a - \frac{1}{1 + i\frac{T_\theta}{T}}\left(b - \mu_{pl}U\right) \qquad (14)$$

and

$$T_\theta = 2\pi\frac{d_c}{V_{pl}}. \qquad (15)$$

Equation (15) represents a characteristic timescale on which the state variable evolves (Ader et al., 2012). From the relationship of $\Delta\tilde{V}e^{i\omega t} = \tilde{V}(t) - \tilde{V}_{pl}$, equations (13) and (14) can be rewritten as $\tilde{V}(t)/\tilde{V}_{pl} = 1 + 2\pi i\Delta\tilde{S}(t)/(\tilde{K}\tilde{V}_{pl} + 2\pi iA)$. We assume that this equation is the Taylor expansion of the RHS of

$$\frac{\tilde{V}(t)}{\tilde{V}_{pl}} = \exp\left(\frac{2\pi i}{\tilde{K}\tilde{V}_{pl} + 2\pi iA}\Delta\tilde{S}(t)\right) \tag{16}$$

to the first order. Then, comparing equation (16) with equation (1), we find that the tidal sensitivity (α) and the phase difference (δ) can be written as

$$\alpha = \mathrm{Re}\left(\frac{2\pi i}{(\tilde{K}\tilde{V}_{pl} + 2\pi iA)\sigma_{eff}^{0}}\right) \tag{17}$$

$$\delta = \arg\left(\frac{2\pi i}{\tilde{K}\tilde{V}_{pl} + 2\pi iA}\right) \tag{18}$$

For $U = 0$, where dilatancy/compaction is neglected, Ader et al. (2012) presented a linearized approximation solution and a numerical solution. We confirmed that equations (13) and (18) are consistent with the nondimensionalized version of equation (3) of Ader et al. (2012), who examined tidal responses for different values of T. However, how the tidal response changes with different values of d_c was not studied in detail for the period of ~12 h, which is the dominant period of tides. Therefore, we examined how the tidal response changes with changes in d_c or T_θ (equation (15)) for this period, since a comparison between our model and observations of the tidal response enables us to infer d_c in the actual geophysical situation. Figures 2a and 2b show α and δ, respectively. In these figures, the solid green line and green dots represent the numerical solution of equation (10) and the approximate solution, respectively. The approximate solution and the numerical solution agree with each other within 15% for most cases. When $T_\theta/T \sim 10^{-1}$, the approximate solution is less accurate for both α and δ. This means that the accuracy of the approximate solution can deteriorate when the nonlinearity is stronger (i.e., α is larger).

For $U \neq 0$, the approximate solution agrees with the numerical solution within 10% for all cases (the deviation between the approximate and numerical solutions is the maximum when $T_\theta/T \sim 140$ and $U = 1$. In this case, $\delta \sim 1.134$ for the numerical solution and $\delta \sim 1.023$ for the approximate solution, resulting in a relative error of ~9.7%). The good agreement is attributed to the fact that α is relatively small (at most ~0.7 kPa^{-1}); thus, the nonlinearity is weaker. This indicates that the approximate solution is valid regardless of the value of T_θ/T when $U \neq 0$.

3.2 Dependence of the tidal response on the fault physical properties

Based on the approximate solution and an analysis of the quasi-static equation of motion, we clarify how α and δ during an ETS depend on the fault physical properties. The specific range of physical properties that can explain the observations is discussed in section 4.

3.2.1 Factors governing the tidal response during the ETS

We assume that the VS region surrounding tremor patches slides at an average velocity of V_{pl}. In our spring-slider model, this situation is represented by setting the velocity of the pulling spring to V_{pl}. We can apply this model to fault creep during the ETS, which occurs over a shorter time span than secular plate subduction. Geodetic observations show that the fault creep velocity during an ETS is $\sim 10^{-6\sim -9}$ m/s (e.g., Meade and Loveless, 2009; Schwartz and Rokosky, 2007). Therefore, we set V_{pl} as 10^{-8} m/s in the following numerical simulation. In addition, the frictional parameters a and b are chosen so that $a-b$ is small because it has been suggested that $a-b$ decreases in the transition zone (e.g., Liu, 2013; Matsuzawa et al., 2010). The other parameters are similar to those used in previous studies (Ader et al., 2012; Hawthorne and Rubin, 2013). Table 2 shows the adopted parameters. For these parameters, we can confirm that $\left|\tilde{K}\tilde{V}_{pl}\right| \ll |2\pi i A|$. Then, the tidal response (equations (17) and (18)) can be approximated as

$$\alpha \sim \mathrm{Re}\left\{\left(A\sigma_{eff}^{0}\right)^{-1}\right\} \tag{19}$$

$$\delta \sim \arg\{A^{-1}\}. \tag{20}$$

Combining these equations with equation (14), we note that α and δ depend on T_θ/T and U. The former parameter T_θ/T prescribes the response of the state variable to the tide, which is uniquely determined once we determine V_{pl}, d_c and T. T_θ/T is constant throughout the tidal cycle. $T_\theta/T \ll 1$ means that the state variable is close to the steady state value (d_c/V) throughout a tidal cycle, and $T_\theta/T \gg \left|b-\mu_{pl}U\right|/a$ means that the state variable is almost constant throughout a tidal cycle (see section 3.2.3 for more details). In the following, we focus on these two parameters, T_θ/T and U, to discuss the tidal response.

3.2.2 A balance of the stress changes

From Figures 2a and 2b, we see a large difference between the cases for $U = 0$ and $U \neq 0$. The reason for this large difference can be understood by using the following equation, which is derived from the quasi-static equation of motion (equation (8)) (for the derivation, see Appendix A):

$$\Delta S(t) \sim \sigma_{eff}^{0} \left(-\mu_{pl} U ln\left(\frac{\theta}{\theta_{pl}}\right) + a ln\left(\frac{V}{V_{pl}}\right) + b ln\left(\frac{\theta}{\theta_{pl}}\right) \right). \quad (21)$$

In equation (21), the left-hand side (LHS) and RHS correspond to the tidal Coulomb stress and frictional strength, respectively. The first, second, and third terms on the RHS represent the dilatancy/compaction effect, the direct effect, and the evolution effect, respectively. When $U = 0$, the first term vanishes, and the tidal response (equations (19) and (20)) obtained in this study is consistent with the result discussed in Chapter 4.1 of Hawthrome and Rubin (2013). Therefore, we analyze the tidal response for $U \neq 0$ below.

3.2.3 Analysis of the tidal response for$U \neq 0$

Figures 2a and 2b show that the tidal response can be classified into three cases according to the value of T_θ/T because the value affects the degree to which the first term of $a\{1 - (b - \mu_{pl}U)/a(1 + iT_\theta/T)\}$ is dominant (see equation (14)). The condition for the first term on the RHS of equation (14) to be negligibly small is $|b - \mu_{pl}U|/a|1 + iT_\theta/T| \ll 1$. Using the parameter set shown in Table 2, we obtain $|b - \mu_{pl}U|/a \sim O(1)$, so $T_\theta/T \gg |b - \mu_{pl}U|/a$ is required for the above inequality to hold. Conversely, the condition for the first term on the RHS of equation (14) becoming dominant is when the value of $a(1 + iT_\theta/T)$ becomes ~a. In other words, $T_\theta/T \ll 1$. The other case is the intermediate region between these two limits.

First, we consider the case where $T_\theta/T \gg |b - \mu_{pl}U|/a$. We find that for larger values of T_θ/T, α and δ converge to the same values regardless of the value of U ($T_\theta/T \sim 10^4$ in Figures 2a and 2b). When $T_\theta/T \gg |b - \mu_{pl}U|/a$, the first term on the RHS of equation (14) can be ignored ($A \sim a$). Therefore, substituting $A \sim a$ into equations (19) and (20), α and δ become $a\sigma_{eff}^{0}$ and 0, respectively, regardless of the value of U. Because the state variable evolves more slowly than the tidal Coulomb stress change, the state variable is almost constant ($\theta \sim \theta_{pl}$) throughout a tidal cycle. Then, the dilatancy/compaction and the evolution effect term of equation (21) are almost zero. Therefore, equation (21) can be approximated as $\Delta S(t) \sim a\sigma_{eff}^{0} \log(V/V_{pl})$ or $V \sim V_{pl} e^{\Delta S(t)/a\sigma_{eff}^{0}}$. This means that $\alpha = 1/a\sigma_{eff}^{0}$.

Moreover, the form of this equation indicates that the slip velocity peak agrees with the tidal Coulomb stress peak in time, which means that $\delta = 0$.

Next, we consider the case where $T_\theta/T \ll 1$. In this case, α depends on U and takes a small value when U is large ($T_\theta/T \sim 10^{-2}$ in Figure 2a). However, δ converges to zero regardless of the value of U ($T_\theta/T \sim 10^{-2}$ in Figure 2b). When $T_\theta/T \ll 1$, we obtain $\alpha = 1/(a - b + \mu_0 U)\sigma_{eff}^0$ and $\delta = 0$ from equations (14), (19) and (20). Because the state variable evolves more rapidly than the tidal Coulomb stress change, the state variable is close to the steady state value ($\theta \sim d_c/V$) throughout a tidal cycle. This is derived by considering $\mathrm{d}\theta/\mathrm{d}t \sim 0$ in equation (4). Then, equation (21) can be approximated as $\Delta S(t) \sim \left(a - b + \mu_{pl} U\right)\sigma_{eff}^0 \log\left(V/V_{pl}\right)$. As before, the form of this equation explains the above values of α and δ. Moreover, it is clear from the form of α that it decreases as U increases.

Finally, we consider the case of the intermediate region between the above two limit cases ($T_\theta/T \ll 1$ and $T_\theta/T \gg \left|b - \mu_{pl} U\right|/a$). Figure 2a shows that α varies smoothly and connects the limit values for $T_\theta/T \gg \left|b - \mu_{pl} U\right|/a$ and $T_\theta/T \ll 1$ ($T_\theta/T \sim 10^{0\sim 1}$ in Figure 2a). Figure 2b shows that the maximum value of δ approaches $\pi/2$ as U increases ($T_\theta/T \sim 10^{0\sim 1}$ in Figure 2b). To clarify why this occurs, we compared the time variation of the tidal Coulomb stress term ($\Delta S(t)$ of equation (21)), the dilatancy/compaction effect term and the evolution effect term in equation (21). Figure 3 shows these three terms for $U = 1$ and $U = 0.01$. For $U = 1$, the amplitude of the dotted blue line representing the tidal Coulomb stress and the amplitude of the solid black line representing the dilatancy/compaction effect are almost the same, and there is a slight phase difference between them. Representing this phase difference as $\beta(\ll \pi)$, we see from the balance between the solid black line and the dot blue line in Figure 3 that $-\mu_{pl} U \sigma_{eff}^0 \log\left(\theta/\theta_{pl}\right) \sim |\Delta S(t)| e^{i\omega(t-\beta)}$. The dashed black line representing the evolution effect is negligibly small ($b\sigma_{eff}^0 \log\left(\theta/\theta_{pl}\right) \sim 0$). Substituting these into equation (21), and after some algebra (Appendix B), we find that

$$\log\left(\frac{V}{V_{pl}}\right) \propto \mathrm{Re}\left\{e^{i\omega\left(t+\frac{\pi}{2}\right)}\right\}. \quad (22)$$

This formula indicates that the slip velocity peak agrees with the tidal Coulomb stress rate peak ($T_\theta/T \sim 10^1$ in the black line of Figure 2a). For $U = 0.01$, the phase difference δ is small ($T_\theta/T \sim 10^0$ in the blue line of Figure 2a). This difference can be explained by considering the balance in equation (21). The amplitude of the solid yellow line representing the dilatancy/compaction effect in equation (21) is smaller than the amplitude of the dotted blue line representing the tidal Coulomb stress. Furthermore, the dashed yellow line representing the evolution effect decreases when the dilatancy/compaction effect term (solid yellow line) is larger and vice versa. Therefore, the amplitude of the sum of these two effects becomes even smaller than the amplitude of $\Delta S(t)$. For the stress balance of equation (21) to be satisfied, the direct effect term (second term on the RHS) should balance the difference between $\Delta S(t)$ and the sum of the above two effects. This means that for a smaller U, a larger direct effect is needed. The dominance of the direct effect term indicates that δ is small, as we have seen for the case of $T_\theta/T \gg \left|b - \mu_{pl}U\right|/a$, which explains why δ is closer to zero for $U = 0.01$ than for $U = 1$, as shown by Figure 2 (Figure S5 shows the time variation of the tidal Coulomb stress term ($\Delta S(t)$ of equation (21)), the dilatancy/compaction effect term and the evolution effect term in equation at $U = 0.1$).

Figure S6 schematically illustrates how the pore fluid (dilatancy/compaction effect), tidal stresses and fault creep velocity generally evolve during one tidal oscillation. Because the case for $U = 1$ can reproduce the observations at both stages of the ETS, we show only the case for $U = 1$.

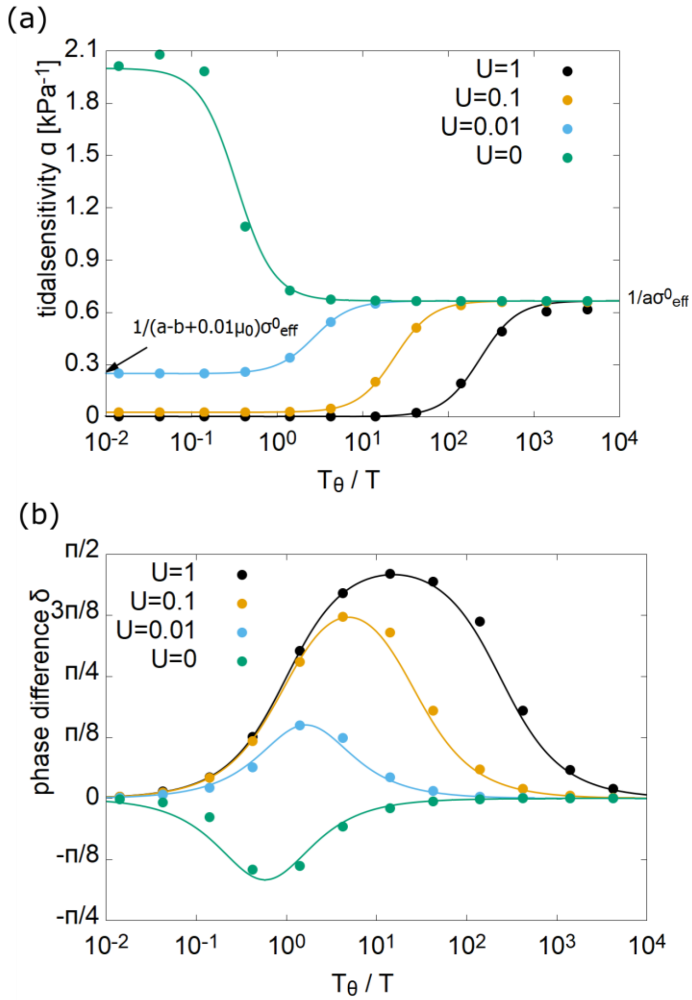

Figure 2. (a) The numerical solution of α (dots) and the approximation solution (equation (19)) (solid line). From equation (19), we can derive $\alpha = 1/(a - b + \mu_0 U)\sigma_{eff}^0$ when $T_\theta/T \ll 1$ and $\alpha = 1/a\sigma_{eff}^0$ when $T_\theta/T \gg \left|b - \mu_{pl}U\right|/a$. Specific values for $U = 0.01$ are displayed in the figure at $T_\theta/T \gg \left|b - \mu_{pl}U\right|/a$ and at $T_\theta/T \ll 1$. (b) The numerical solution of δ (dots) and the approximation solution (equation (20)) (solid line). The differences in color represent the differences in the dilatancy parameter U.

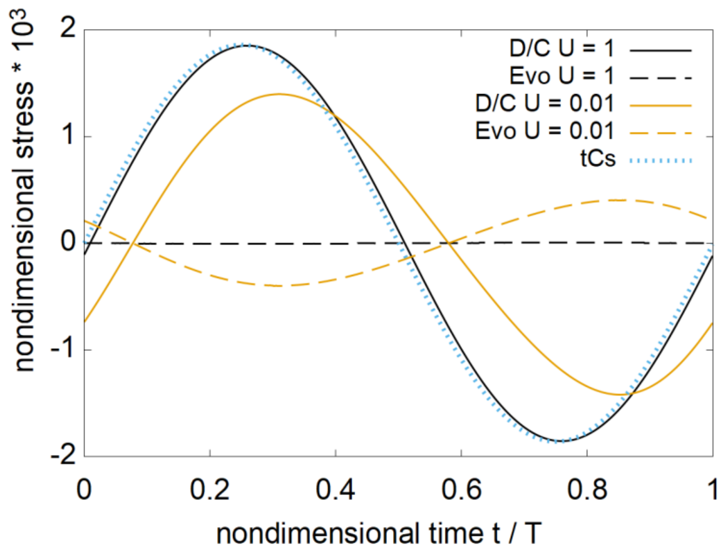

Figure 3. Time evolution of the tidal Coulomb stress (tCs) (blue dotted line), the dilatancy/compaction effect (D/C) (solid lines), and the evolution effect (Evo) (dashed lines) in equation (21). The horizontal axis denotes time normalized by the tidal cycle, and the values from 0 to 1 indicate one tidal cycle. The vertical axis denotes the tidal Coulomb stress/frictional strength normalized by σ_{eff}^0. The numerical solutions for $T_\theta/T = 14$ and $U = 1$ are shown in black, and those for $T_\theta/T = 1.4$ and $U = 0.01$ are shown in yellow.

4 Discussion

4.1 Application of the model to the observed tidal response during the ETS

As mentioned in the introduction, most of the previous models are unable to account for the phase difference of $\delta \sim \pi/2$, which is observed at the early stage of ETS. As shown below, our model reproduces the tidal response during the ETS, including the phase difference, for a specific range of fault physical properties constrained by experiments, geological studies, and numerical modeling.

The observed tidal responses typically show $\alpha \lesssim 0.1$ kPa^{-1} and $\delta \sim \pi/2$ at the early stage of the ETS and $\alpha \sim 0.7$ kPa^{-1} and $\delta \sim 0$ at the later stage of the ETS. The slip velocity of the fault, which rapidly increases at the onset of the ETS, decreases to below steady-state subduction velocity with the progress of the ETS. In our model, ETS is represented by setting V_{pl} higher than the steady-state subduction velocity (Table 2). Considering that

$V_{pl}\sim10^{-8\sim-6}$ m/s, at the moment, we assume $V_{pl}\sim10^{-6}$ m/s at the early stage of the ETS and $V_{pl}\sim10^{-8}$ m/s at the later stage.

4.2.1 The ranges of U reproduce the observation

We see from Figure 2a and 2b that the model reproduces the observed tidal response at the early stage of ETS ($\alpha \lesssim 0.1,\ \delta\sim\pi/2$) when $T_\theta/T\sim10$ and $U\sim1$. This case corresponds to the last of the three categories of T_θ/T presented in section 3.2.3. We have seen that the first term on the RHS of equation (21) (the dilatancy/compaction effect term), which has a phase delay with respect to the tidal Coulomb stress change, dominates in the frictional strength change, and δ becomes $\pi/2$. The dominance of the dilatancy/compaction effect term reduces the direct effect term, which results in a smaller variation in the slip velocity ($\alpha \lesssim 0.1$). For $V_{pl} = 10^{-6}$ m/s, we obtain $d_c = 10^{-1}$ m from the condition of $T_\theta/T\sim10$ (equation (15)).

Up to this point, we have used the undrained model. The drained model assumes that the pore fluid pressure diffuses outside the shear zone, as shown in equation (S1). This implies that the shear zone has a high permeability. From text S1 and S2 in the supporting information, we derived the dilatancy parameter (E_p) in the drained model and estimated the valid range of the parameter. Within the range, the drained model can reproduce α for both the initial and later stages by assuming $d_c = 10^{-2}$ m (the solid black line in Figure S3a in the supporting information). However, the drained model cannot reproduce $\delta\sim\pi/2$ at the early stage (Figure S3b in the supporting information). In addition, we confirmed that even when the dilatancy parameter is an order of magnitude larger than the reasonable value, we cannot reproduce $\delta\sim\pi/2$ at the early stage (Figure S7 in the supporting information). The result that only the undrained model can reproduce both α and δ suggests the low permeability of the shear zone. This indicates the possibility that our model can constrain the frictional parameters and the dilatancy coefficient as well as a hydraulic property of the fault through a comparison with observations of tidal response.

Here, we return to the application of the undrained model. Focusing on the case of $U\sim1$, which explains the early stage, we see that the model can reproduce the observed tidal response at the later stage of the ETS ($\alpha\sim0.7$ kPa^{-1} and $\delta\sim0$) when $T_\theta/T \gtrsim 10^3$. This case corresponds to $T_\theta/T \gg \left|b-\mu_{pl}U\right|/a$ described in the three categories in section 3.2.3. As noted above, the phase advance disappears ($\delta\sim0$) as the direct effect term (second term) on the RHS of equation (21) becomes dominant in the frictional strength change, and α asymptotically reaches a value that is independent of U ($\alpha\sim1/a\sigma_{eff}^0$). For $V_{pl} = 10^{-8}$ m/s, the condition of $T_\theta/T \gtrsim 10^3$ indicates that $d_c \gtrsim 10^{-1}$ m.

On the other hand, Figure 2a shows that the model for $U = 0.01$ and $U = 0.1$ can explain the tidal response at the later stage of ETS when $d_c \gtrsim 10^{-3}$ m and $d_c \gtrsim 10^{-2}$ m, respectively. This means that if we apply the model only to the tidal response at the later stage of ETS, d_c might be underestimated.

The above comparison between the model and observations shows that the dilatancy/compaction effect is dominant at the early stage of the ETS, while the dilatancy/compaction effect is negligible at the later stage of the ETS. Figure 4 schematically illustrates the physical process suggested by our model. First, we see the early stage of ETS (Figure 4a). A higher tide level increases the ocean load and reduces $\Delta S(t)$. At low tide ($\delta \sim 0$), $\Delta S(t)$ takes its maximum. However, the effect generated by the low tide is almost canceled out by the significant increase in the normal stress due to the dilatancy/compaction effect. At the mean tide ($\delta \sim \pi/2$), $\Delta S(t)$ is zero. The dilatancy/compaction effect is reduced but still able to decrease the normal stress. Consequently, the slip velocity or the tremor rate reaches the maximum. Next, we see the later stage of ETS (Figure 4b). Since the dilatancy/compaction effect is always negligible at this stage, the slip velocity is maximized when $\Delta S(t)$ becomes the largest (low tide).

Incidentally, we can reproduce the observed tidal response (α, δ) as well as the observation that the number of tremors decreases by one or two orders of magnitude at the later stage of ETS compared to that at the early stage. This is because in equation (2), the tremor rate is proportional to the fault creep velocity, meaning that the tremor rate at the later stage of the ETS ($V_{pl} \sim 10^{-8}$ m/s) is two orders of magnitude less than the tremor rate at the early stage of the ETS ($V_{pl} \sim 10^{-6}$ m/s).

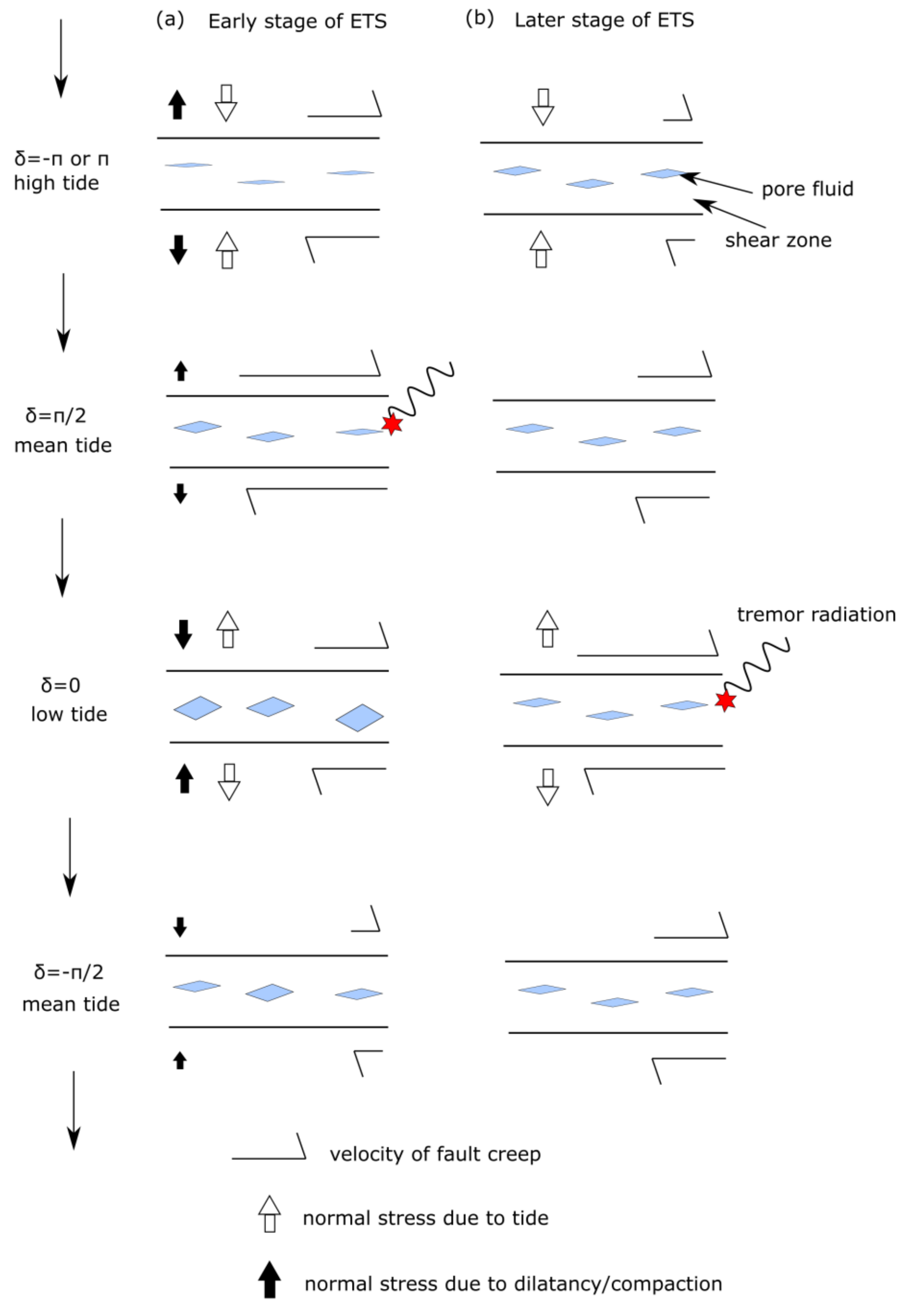

Figure 4. A schematic illustration of the relationship between the fault creep velocity and tide level. For simplicity, only the normal stress change is represented. (a) Early stage of ETS. The sum of the normal stress due to the dilatancy/compaction effect (black arrows) and the tidal normal stress (white arrows) becomes the largest in the sense of enhancing fault slip at $\delta \sim \pi/2$. (b) Later stage of ETS. The dilatancy/compaction effect is negligible, and the fault creep velocity reaches its maximum at $\delta \sim 0$.

4.2.2 The ranges of d_c reproduce the observation

In section 4.2.1, we showed that the observation can be reproduced when $d_c \sim 10^{-1}$ m, assuming $V_{pl} \sim 10^{-8\sim-6}$ m/s. On the other hand, Figure 5 (a) and (b) show that the observation cannot be reproduced when d_c is other than ~10^{-1} m. For example, when $d_c = 10^{-3}$, $\alpha \sim 0$ and $\delta \sim 0$ at the early stage of ETS ($V_{pl} \sim 10^{-6}$ m/s) and $\alpha \sim 0$ and $\delta \sim \pi/2$ at the later stage of ETS ($V_{pl} \sim 10^{-8}$ m/s).

The above range of $d_c \sim 10^{-1}$ m, which explains the observation, was determined from the conditions that $T_\theta/T \sim 10$ at the early stage of ETS and $T_\theta/T \gg |b - \mu_{pl}U|/a$ (~100) at the later stage of ETS. In principle, these two conditions can be met for any V_{pl} if d_c is appropriately chosen, considering the form of equation (15). In practice, however, d_c can be constrained based on V_{pl} estimated from observations and numerical simulations. Based on observations and simulations, the slip velocity of the SSE is $10^{-9\sim-6}$ m/s (e.g., Goswami and Barbot 2018; Schwartz and Rokosky, 2007; Segall et al. 2010). The slip velocity of the fault, which rapidly increases at the onset of the ETS, decreases to the inter-ETS period velocity with the progress of the ETS. Based on the above conditions, we can reproduce the observation not only for $V_{pl} \sim 10^{-8\sim-6}$ m/s but also for $V_{pl} \sim 10^{-9\sim-7}$ m/s by employing $d_c = 10^{-2}$ (Figure S8). When d_c is other than 10^{-2} m, the observation cannot be reproduced.

Therefore, our model and observations are consistent for critical slip distances of 0.1-0.01 m in the transition zone.

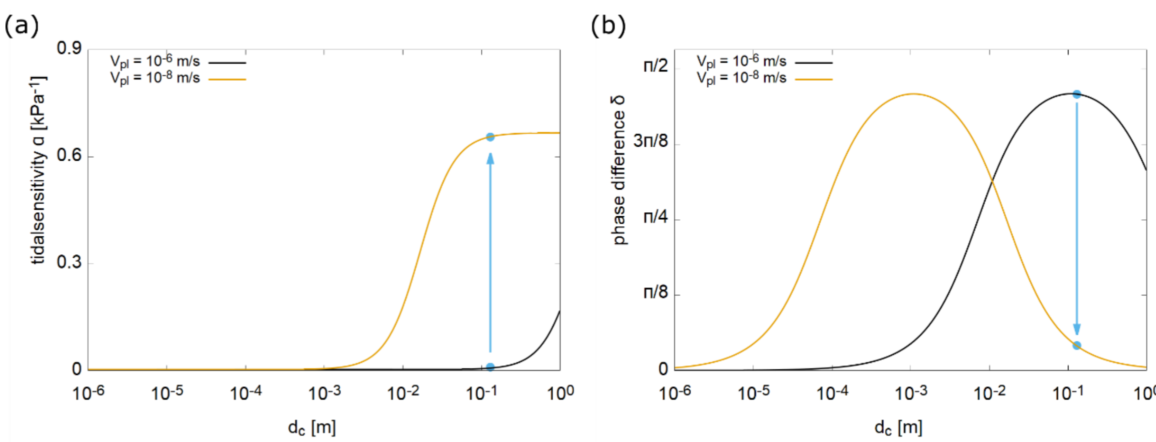

Figure 5. (a) The approximation solution of α (equation (19)) when $V_{pl} = 10^{-6}$ m/s (black) and 10^{-8} m/s (yellow). The horizontal axis denotes the critical slip distance d_c. The blue dots show that α for $d_c = 0.13$ m increases from $\lesssim 0.1$ to ~ 0.7 as V_{pl} decreases from 10^{-6} m/s to 10^{-8} m/s. (b) The

same as in (a) but for the approximation solution of δ (equation (20)). The blue dots show that δ decreases from $\sim\pi/2$ to ~ 0 as V_{pl} decreases from 10^{-6} m/s to 10^{-8} m/s.

4.3 The constrained physical fault properties

For our model to simultaneously reproduce the observed tidal responses at the early and later stages of the ETS, the following four conditions must be satisfied: $U\left(= M\epsilon/\sigma_{eff}^{0}\right)\sim 1$, $d_c \sim 10^{-1}$ m, the occurrence of dilatancy/compaction in the fault creep region (i.e., $a > b$) and low permeability within the shear zone (undrained model). Below, we discuss the validity of these conditions.

4.3.1 The dilatancy parameter U

Samuelson et al. (2009) obtained a dilatancy coefficient, and Segall et al. (1995) obtained bulk moduli of the fluid and pore space. These results yield $\epsilon \sim 10^{-4\sim-5}$ and $M \sim 10^{10}$ Pa (equation (7)). We assume that these experimentally obtained values are of the same magnitude in the transition zone. Substituting these values into $U\left(= \epsilon M/\sigma_{eff}^{0}\right) = 1$, which reproduces the observed tidal response, we obtain $\sigma_{eff}^{0} = \epsilon M U \sim 10^{5\sim 6}$ Pa, which supports a near-lithostatic pore fluid pressure (e.g., Audet et al., 2009; Nakata, 2008; Shelly et al., 2006; Yabe et al., 2015).

4.3.2 The critical slip distance d_c

The results of friction experiments on rocks and gouges show $d_c \sim 10^{-4\sim-6}$ m (e.g., Marone, 1998). Our results ($d_c \sim 10^{-1\sim 2}$ m) are $2\sim 5$ orders of magnitude larger. The much larger critical slip distance can be explained by considering the differences in roughness between laboratory surfaces and natural faults (Scholz et al., 1988) and the differences in the thickness of the shear zone between experimental and natural faults (Marone and Kilgore, 1993).

Numerical models assuming the RSF also adopt a critical slip distance larger than that in the experimental results. For example, Nakata et al. (2012) successfully modeled the SSE and aftershocks after the ~M7 earthquake in Hyuga-nada, Japan, with $d_c = 10^{-1\sim 0}$ m. Maury et al. (2014) calculated a time evolution of shear stress for the SSE in Mexico and estimated that the critical slip distance that can quantitatively reproduce the observed results is 5×10^{-2} m. Kawamura et al. (2018) applied a 1-D multidegree of freedom spring-slider model with $d_c = 10^{-2}$ m to reproduce various types of fault slip, such as fast slip, source nucleation, aftershock, and SSE. Our analysis of the tidal response during ETS also supports d_c with the order of $10^{-1\sim-2}$ m.

4.3.3 The occurrence of dilatancy/compaction in the fault creep region

Numerical models that have been proposed thus far generally require the presence of a VW region $(a-b<0)$ to reproduce SSE (e.g., Liu and Rice, 2005; Segall et al., 2010). Some models have proposed a mechanism by which SSE occurs in the VS regime, such as the generation of a negative Coulomb stress change due to fault valve action (Perfettini and Ampuro 2008) and the transition of the RSF from the VW at low speeds to the VS at high speeds (e.g., Im et al., 2020; Peng and Rubin, 2018; Shibazaki and Iio. 2003). Our model employs the framework of the VS and expresses the velocity of the slow slip by V_{pl} phenomenologically.

The above two models assuming the VS (e.g., Im et al., 2020; Peng and Rubin, 2018; Perfettini and Ampuro, 2008; Shibazaki and Iio 2003) do not consider the time variation of pore fluid pressure. On the other hand, Beeler et al. (2018) developed a model that considers the time variation of pore fluid pressure in the VW region. However, it cannot be applicable to the tidal modulation of the tremor rate during ETS. Our results show that when we assume the framework of the VS, the observed tidal response at the early stage of ETS cannot be reproduced unless dilatancy/compaction occurs.

4.3.4 The fluid pressure diffusivity derived from the undrained condition

For the undrained model, $T \ll t_w$ must be satisfied (section 2.2.2). Using this condition, we can quantitatively constrain the fluid pressure diffusivity as follows. We assume that the thickness of the shear zone is w and the fluid pressure diffusivity in the shear zone is c^*_{hyd}. Then, a dimensional analysis shows that $w \sim \sqrt{t_w c^*_{hyd}}$, where t_w denotes the characteristic timescale on which the pore fluid pressure diffuses through the shear zone. Therefore, the condition of $T \ll t_w$ can be rewritten as $T \ll w^2/c^*_{hyd}$.

We estimate w in the transition zone in the following manner since it cannot be observed directly. A drilling investigation and structural analyses of drill cores on the Nojima Fault revealed that w in the seismogenic zone is $\sim 10^{1/2}$ m (Lin and Nishikawa, 2019). It is generally expected that w in the VS region is larger than in the VW region (e.g., Chen and Rampel, 2015). Therefore, we assume $w \sim 10^{0\sim1/2}$ m in the VS region. Then, the above undrained condition yields $c^*_{hyd} \ll 2 * 10^{-5\sim-4}\ \mathrm{m}^2/\mathrm{s}$. This value of c^*_{hyd} is consistent with Branut (2021), who reported that the observed rupture propagation of an SSE could be reproduced by a crack propagation model at $w \sim 6\ cm$ and $c^*_{hyd} \sim 10^{-6}\ \mathrm{m}^2/\mathrm{s}$. Previous studies have shown that the c^*_{hyd} of the seismogenic zone is $\sim 10^{-8 \sim -3}\ \mathrm{m}^2/\mathrm{s}$ (Yamashita and Tsutsumi, 2018). Our results suggest that the shear zone in the transition zone is probably as impermeable as that in the seismogenic zone.

4.4 Other effects than dilatancy/compaction

We have seen that the dilatancy/compaction effect is important to explain the phase difference $(\delta \sim \pi/2)$ in the tidal response. In this section, we examine whether other effects could explain $\delta \sim \pi/2$. The following two possibilities are considered.

In the first case, a change in the state variable is introduced due to the normal stress acting on the fault plane (Linker and Dieterich, 1992). In this case, the time variation of the state variable can be written as follows:

$$\frac{d\theta}{dt} = -\frac{V\theta}{d_c}\log\left(\frac{V\theta}{d_c}\right) - \frac{\gamma}{b}\frac{\dot{\sigma}}{\sigma}\theta, \qquad (23)$$

where γ is a constitutive parameter representing a normal stress dependence. In general, $\gamma \sim O(0.1)$. Therefore, we adopt $\gamma = 0.2$ and solve the governing equations of our model replacing the evolution law (equation (4)) with equation (23). The results indicate that the difference caused by considering the effect of normal stress on the state variable is less than 1%. Therefore, the influence of the Linker-Dieterich effect is small and does not provide a reason for the large phase difference.

In the second case, tidal Coulomb stress can directly destroy the tremor source instead of aseismic slip on the surrounding fault. This effect is ignored in our model. If this is the case, the tremor rate is proportional to the tidal Coulomb stressing rate (i.e., $\delta \sim \pi/2$) (Beeler et al., 2013; Lockner and Beeler, 1999). This direct effect of the tidal Coulomb stress should become clearer when the aseismic slip on the surrounding fault is smaller, i.e., at the later stage of the ETS (Royer et al., 2015). However, the observed result shows $\delta \sim 0$ at the later stage, indicating that the direct effect is smaller.

None of the above effects can explain the phase difference of $\delta \sim \pi/2$, and thus, the pore fluid pressure change due to dilatancy/compaction is more likely to cause the large phase difference at the early stage of the ETS.

4.5 Application to the tidal response of continuous families

By setting the value of V_{pl} to a steady-state plate convergence velocity (e.g., 10^{-9} m/s), we can examine the range of d_c and U in which our model reproduces the tidal response of continuous families. The observations show that the tidal response of continuous families is $\delta \sim 0$ (Ide and Tanaka, 2014; Thomas et al., 2012) and $\alpha \sim 1.5$ kPa^{-1} (Thomas et al., 2012), for example. We examine whether these observations can be reproduced with parameters that reproduce the tidal response of episodic families ($d_c \sim 10^{-1}$ m, $U \sim 1$) (section 4.2). In the case of $d_c = 10^{-1}$ m, $V_{pl} = 10^{-9}$ m/s and $T_\theta/T \sim 10^4$, we obtain $\alpha \sim a\sigma_{eff}^0 (= 0.67$ kPa$^{-1})$ and $\delta \sim 0$ (section 3.2.2). Therefore, by slightly reducing the value of σ_{eff}^0, the tidal responses of continuous families and episodic families can be reproduced with similar values of the fault physical properties.

4.6 Limitations of our model

Our model, in which fault creep is represented with a one-degree-of-freedom spring block of the VS regime ($a - b > 0$), necessarily fails to include the occurrence of slow slip accompanying a rapid release of the accumulated stress. For this reason, we expressed the occurrence of slow slip by the difference in V_{pl} and assumed that the tremor rate during ETS is proportional to the fault creep velocity (equation (2)). Our model accounted for the tidal response of tremors during ETS, but this does not hold if the frictional law requires $a - b < 0$ during SSE. In such a case, our model needs to be extended to include unstable regions ($a - b < 0$) by increasing the degrees of freedom.

Models that assume $a - b < 0$, which have been proposed thus far, include models with complex fault geometries (Romanet et al., 2018), 3-D elastic media (Matsuzawa et al., 2010), heterogeneous fault physical properties (Luo and Ampuero, 2018), and nonuniform permeability in space and time (Bizzarri, 2012; Cappa, 2011; Dunham and Rice, 2008). They account for more complex effects that are not considered in our model. However, the tidal response of these models has not yet been investigated.

Because our model adopts a one-degree-of-freedom (one-DOF) spring-slider system, it cannot simulate the spatiotemporal variation in stress during an ETS. Such spatiotemporal changes in stress have been modeled using a two-dimensional system (e.g., Hawthorne and Rubin, 2013), which can reproduce observations such as a spatial propagation of ETS and temporal changes in the slip velocity during ETS. Hawthorne and Rubin (2013) examined the tidal response of ETS based on such a 2-D model.

However, Hawthorne and Rubin (2013) reported that the tidal response during ETS obtained by a 2-D simulation qualitatively agrees with the tidal response of the one-DOF ramp block slider model. Their model does not include the effect of dilatancy/compaction. To confirm whether the one-DOF and 2-D simulation results are in agreement for a model including the dilatancy/compaction effect, we need to extend our model to a 2-D system. One approach to do so would be to incorporate the dilatancy/compaction effect considered in our model into the model of Hawthorne and Rubin (2013).

5 Conclusions

Tremors in the transition zone are sensitive to tidal stress. In this study, we propose a physical model to explain the tidal response of tremors observed during the ETS. Following previous studies (Ader et al., 2012; Beeler et al., 2013; Shelly et al., 2007a), we assumed that tremors are generated by the rupture of a small brittle patch on the fault plane due to the aseismic shear slip of a larger-scale surrounding fault. As in Ader et al. (2012), we adopted a one-degree-of-freedom spring-slider that follows the RSF for the VS and set up the governing equations to describe the slip behavior of the block, considering a pore fluid pressure change in the shear zone (section 2). We considered drained (high-permeability) and undrained (low-permeability) models and presented results are mainly of the undrained model, which could reproduce more observations than the drained model. The inclusion of pore pressure changes due to dilatancy/compaction in the VS regime is in remarkable contrast to previous theoretical models describing tidal modulation.

In our model, the tidal response is expressed with the tidal sensitivity (α), which represents the amplitude of the tidal modulation of fault creep velocity, and the phase difference (δ) of the fault creep velocity peak relative to the tidal Coulomb stress peak. We analytically derived an approximate solution to reveal how the tidal response depends on the fault physical properties in section 3. We note that the slip behavior is primarily controlled by the characteristic timescale $T_\theta \left(= 2\pi d_c/V_{pl}\right)$ at which the state variable evolves, where d_c is the critical slip distance and V_{pl} is the background fault creep. We found that the behavior of α and δ can be classified into three cases according to the magnitude of T_θ/T ($T_\theta/T \gg \left|b - \mu_{pl}U\right|/a, T_\theta/T \sim 1 \sim \left|b - \mu_{pl}U\right|/a,\ T_\theta/T \ll 1$), where T is the tidal cycle (~12 hours), a and b are frictional constitutive parameters, μ_{pl} is the frictional coefficient and U is the dilatancy parameter. This classification reflects the degree to which the dilatancy/compaction effect is dominant in the frictional strength change. We showed that the smaller T_θ/T is, the more dominant the dilatancy/compaction effect is in the friction strength change.

We applied the model to ETS, assuming that V_{pl} changes between the early and later stages of the ETS. The model successfully reproduced the tidal response observed at both stages of the ETS. Adopting this undrained model, we constrained the effective normal stress to be $10^{5\sim6}$ Pa, the critical slip distance to be $10^{-1\sim-2}$ m, and the fluid pressure diffusivity to be 10^{-5} $\mathrm{m^2/s}$ or less. Of particular importance is the use of the phase difference in the estimation of the fault properties. Without considering the dilatancy/compaction effect, the phase difference at the early stage cannot be reproduced. Moreover, using the tidal response data obtained during only the early stage or the later stage produces different estimates of the fault properties. The range of the fault properties obtained in our study are in the ranges inferred by independent studies. Our model supports a critical slip distance of ~$10^{-1\sim-2}$ m, which has been used in numerical simulations of earthquake cycles. This study shows that the physical modeling of the tidal response of tremors during the ETS is an effective method to retrieve the fault properties in the transition zone, including hydraulic properties.

Appendices

Appendix A: Derivation of equation (21)

Substituting equation (3) into equation (8) and transforming the result, we obtain

$$k\Delta u + \Delta\tau = \left\{\mu_0 + a\log\left(\frac{V_{pl}}{V_0}\right) + b\log\left(\frac{\theta_{pl}}{\theta_0}\right) + a\log\left(\frac{V}{V_{pl}}\right) + b\log\left(\frac{\theta}{\theta_{pl}}\right)\right\}\sigma_{eff}$$

$$= \left\{\mu_{pl} + a\log\left(\frac{V}{V_{pl}}\right) + b\log\left(\frac{\theta}{\theta_{pl}}\right)\right\}\sigma_{eff}. \qquad (A)$$

We represent the relative displacement of the block at the steady state without the tide as Δu_{no}. Then, $k\Delta u_{no} = \mu_{pl}\sigma_{eff}^0$ holds, where the RHS is obtained by setting $\Delta\sigma(t) = 0$ and $\Delta p(t) = 0$ in equation (9). We can confirm that $k\Delta u \sim \mu_{pl}\sigma_{eff}^0$ as follows. For the parameter set in Table 2, $k\Delta\dot{u} \sim O(kV_{pl})$ is three orders of magnitude smaller than $\Delta\dot{\tau} \sim O(2\pi|\Delta\tau|/T)$. This means that $k\Delta\dot{u}$ on the LHS of the time derivative of equation (A) is negligibly small, suggesting that $\Delta u \sim \Delta u_{no}$. Replacing $k\Delta u$ with $\mu_{pl}\sigma_{eff}^0$ on the LHS and using equations (9) and (11), equation (A) can be rewritten as

$$\Delta S(t) = -\mu_{pl}\Delta p(t) + a\sigma_{eff}\log\left(\frac{V}{V_{pl}}\right) + b\sigma_{eff}\log\left(\frac{\theta}{\theta_{pl}}\right). \tag{B}$$

In equation (B), the LHS corresponds to the tidal Coulomb stress and the RHS corresponds to the frictional strength. Furthermore, equation (B) can be written as

$$\Delta S(t) \sim -\mu_{pl}U\sigma_{eff}^{0}\log\left(\frac{\theta}{\theta_{pl}}\right) + a\sigma_{eff}^{0}\log\left(\frac{V}{V_{pl}}\right) + b\sigma_{eff}^{0}\log\left(\frac{\theta}{\theta_{pl}}\right) \tag{C}$$

by using equation (7), where $\Delta p = 0$ is taken at $\theta = \theta_{pl}$, and it is assumed that the changes in the effective normal stress in the second and third terms on the RHS of equation (C) are sufficiently small compared to σ_{eff}^{0}.

Appendix B: Derivation of equation (22)

Substituting $-\mu_{pl}U\sigma_{eff}^{0}\log(\theta/\theta_{pl}) \sim \Delta S e^{i\omega(t-\beta)}$ and $b\sigma_{eff}^{0}\log(\theta/\theta_{pl}) \sim 0$ into equation (21), as described in section 3.2.3, we obtain

$$\log\left(\frac{V}{V_{pl}}\right) \sim |\Delta S(t)|\mathrm{Re}\left(e^{i\omega t} - e^{i\omega(t-\beta)}\right). \tag{D}$$

When $\theta_1 = \omega t - \beta/2, \theta_2 = \beta/2$, we can write $Re\left(e^{i\omega t} - e^{i\omega(t-\beta)}\right) = \cos(\theta_1 + \theta_2) - \cos(\theta_1 - \theta_2) = \sin(\theta_1)\sin(\theta_2)$. Using $\sin(\theta_1) = \cos(\pi/2 + \theta_1)$, we obtain $\sin(\theta_1)\sin(\theta_2) = \cos(\omega t + (\pi - \beta)/2)\sin(\beta/2)$. That is, $\log(V/V_{pl}) \sim |\Delta S(t)|\sin(\beta/2)\cos(\omega t + (\pi - \beta)/2)$. Furthermore, since $\beta \ll \pi$, equation (D) can be rewritten as

$$\log\left(\frac{V}{V_{pl}}\right) \sim |\Delta S(t)|\sin\left(\frac{\beta}{2}\right)\mathrm{Re}\left\{e^{i\left(\omega t + \frac{\pi}{2}\right)}\right\}. \tag{E}$$

Open Research

The source code is available from zenodo (10.5281/zenodo.6403829).

Acknowledgments

We thank Dr. Takehito Suzuki for the valuable discussion of an earlier version of this work. We acknowledge Associate Editor, Kate Huishuan Chen, and the anonymous reviewer for their comments that helped us improve the article. For this study, we used the computer systems of the Earthquake and Volcano Information Center of the Earthquake Research Institute, The University of Tokyo. This work was supported by JSPS KAKENHI Grant Numbers JP16H02219, JP16H06474, JP21H01187 and JP21H05204.

References

Ader, T. J., Ampuero, J. P., & Avouac, J. P. (2012). The role of velocity-neutral creep on the modulation of tectonic tremor activity by periodic loading. *Geophysical research letters, 39*(16). https://doi.org/10.1029/2012GL052326

Audet, P., Bostock, M. G., Christensen, N. I., & Peacock, S. M. (2009). Seismic evidence for overpressured subducted oceanic crust and megathrust fault sealing. *Nature*, *457*(7225), 76-78. https://doi.org/10.1038/nature07650

Audet, P., & Bürgmann, R. (2014). Possible control of subduction zone slow-earthquake periodicity by silica enrichment. *Nature, 510*(7505), 389-392. https://doi.org/10.1038/nature13391

Bartlow, N. M., Lockner, D. A., & Beeler, N. M. (2012). Laboratory triggering of stick‐slip events by oscillatory loading in the presence of pore fluid with implications for physics of tectonic tremor. *Journal of Geophysical Research: Solid Earth*, *117*(B11). https://doi.org/10.1029/2012JB009452

Bartlow, N. M., Miyazaki, S. I., Bradley, A. M., & Segall, P. (2011). Space-time correlation of slip and tremor during the 2009 Cascadia slow slip event. *Geophysical Research Letters*, *38*(18). https://doi.org/10.1029/2011GL048714

Beeler, N. M., & Lockner, D. A. (2003). Why earthquakes correlate weakly with the solid Earth tides: Effects of periodic stress on the rate and probability of earthquake occurrence. *Journal of Geophysical Research: Solid Earth*, *108*(B8). https://doi.org/10.1029/2001JB001518

Beeler, N. M., Thomas, A., Bürgmann, R., & Shelly, D. (2013). Inferring fault rheology from low-frequency earthquakes on the San Andreas. *Journal of Geophysical Research: Solid Earth*, *118*(11), 5976-5990. https://doi.org/10.1002/2013JB010118

Beeler, N. M., Thomas, A., Bürgmann, R., & Shelly, D. (2018). Constraints on friction, dilatancy, diffusivity, and effective stress from low-frequency earthquake rates on the deep San Andreas Fault. *Journal of Geophysical Research: Solid Earth*, *123*(1), 583-605. https://doi.org/10.1002/2017JB015052

Bizzarri, A. (2012). Effects of permeability and porosity evolution on simulated earthquakes. *Journal of structural geology*, *38*, 243-253. https://doi.org/10.1016/j.jsg.2011.07.009

Brantut, N. (2021). Dilatancy toughening of shear cracks and implications for slow rupture propagation. *Journal of Geophysical Research: Solid Earth*, *126*(11), e2021JB022239. https://doi.org/10.1029/2021JB022239

Cappa, F. (2011). Influence of hydromechanical heterogeneities of fault zones on earthquake ruptures. *Geophysical Journal International*, *185*(2), 1049-1058. https://doi.org/10.1111/j.1365-246X.2011.04994.x

Chanard, K., Nicolas, A., Hatano, T., Petrelis, F., Latour, S., Vinciguerra, S., & Schubnel, A. (2019). Sensitivity of acoustic emission triggering to small pore pressure cycling perturbations during brittle creep. *Geophysical Research Letters, 46*(13), 7414-7423. https://doi.org/10.1029/2019GL082093

Chen, J., & Rempel, A. W. (2015). Shear zone broadening controlled by thermal pressurization and poroelastic effects during model earthquakes. *Journal of Geophysical Research: Solid Earth*, *120*(7), 5215-5237. https://doi.org/10.1002/2014JB011641

Chen, K. H., Tai, H. J., Ide, S., Byrne, T. B., & Johnson, C. W. (2018). Tidal modulation and tectonic implications of tremors in Taiwan. *Journal of Geophysical Research: Solid Earth*, *123*(7), 5945-5964. https://doi.org/10.1029/2018JB015663

Cochran, E. S., Vidale, J. E., & Tanaka, S. (2004). Earth tides can trigger shallow thrust fault earthquakes. *Science*, *306*(5699), 1164-1166. 10.1126/science.1103961

Dieterich, J. H. (1979). Modeling of rock friction: 1. Experimental results and constitutive equations. *Journal of Geophysical Research: Solid Earth*, *84*(B5), 2161-2168. https://doi.org/10.1029/JB084iB05p02161

Dragert, H., Wang, K., & James, T. S. (2001). A silent slip event on the deeper Cascadia subduction interface. *Science*, *292*(5521), 1525-1528. https://doi.org/10.1126/science.1060152

Dunham, E. M., & Rice, J. R. (2008). Earthquake slip between dissimilar poroelastic materials. *Journal of Geophysical Research: Solid Earth*, *113*(B9). https://doi.org/10.1029/2007JB005405

Goswami, A., & Barbot, S. (2018). Slow-slip events in semi-brittle serpentinite fault zones. *Scientific reports*, *8*(1), 1-11. https://doi.org/10.1038/s41598-018-24637-z

Hawthorne, J. C., & Rubin, A. M. (2013). Tidal modulation and back-propagating fronts in slow slip events simulated with a velocity-weakening to velocity-strengthening friction law. *Journal of Geophysical Research: Solid Earth*, *118*(3), 1216-1239. https://doi.org/10.1002/jgrb.50107

Heaton, T. H. (1982). Tidal triggering of earthquakes. *Bulletin of the Seismological Society of America*, *72*(6A), 2181-2200. https://doi.org/10.1785/BSSA07206A2181

Hirose, H., Hirahara, K., Kimata, F., Fujii, N., & Miyazaki, S. I. (1999). A slow thrust slip event following the two 1996 Hyuganada earthquakes beneath the Bungo Channel, southwest Japan. *Geophysical Research Letters*, *26*(21), 3237-3240. https://doi.org/10.1029/1999GL010999

Hirose, H., & Obara, K. (2010). Recurrence behavior of short-term slow slip and correlated nonvolcanic tremor episodes in western Shikoku, southwest Japan. *Journal of Geophysical Research: Solid Earth*, *115*(B6). https://doi.org/10.1029/2008JB006050

Houston, H. (2015). Low friction and fault weakening revealed by rising sensitivity of tremor to tidal stress. *Nature Geoscience*, *8*(5), 409-415. https://doi.org/10.1038/ngeo2419

Ide, S. (2010). Striations, duration, migration and tidal response in deep tremor. *Nature*, *466*(7304), 356-359. https://doi.org/10.1038/nature09251

Ide, S., Shelly, D. R., & Beroza, G. C. (2007). Mechanism of deep low frequency earthquakes: Further evidence that deep non-volcanic tremor is generated by shear slip on the plate interface. *Geophysical Research Letters*, *34*(3). https://doi.org/10.1029/2006GL028890

Ide, S., & Tanaka, Y. (2014). Controls on plate motion by oscillating tidal stress: Evidence from deep tremors in western Japan. *Geophysical Research Letters*, *41*(11), 3842-3850. https://doi.org/10.1002/2014GL060035

Ide, S., Yabe, S., Tai, H. J., & Chen, K. H. (2015). Thrust-type focal mechanisms of tectonic tremors in Taiwan: Evidence of subduction. *Geophysical Research Letters*, *42*(9), 3248-3256. https://doi.org/10.1002/2015GL063794

Im, K., Saffer, D., Marone, C., & Avouac, J. P. (2020). Slip-rate-dependent friction as a universal mechanism for slow slip events. *Nature Geoscience*, *13*(10), 705-710. https://doi.org/10.1038/s41561-020-0627-9

Ito, Y., Obara, K., Shiomi, K., Sekine, S., & Hirose, H. (2007). Slow earthquakes coincident with episodic tremors and slow slip events. *Science*, *315*(5811), 503-506. https://doi.org/10.1126/science.1134454

Kawamura, H., Yamamoto, M., & Ueda, Y. (2018). Slow-Slip Phenomena Represented by the One-Dimensional Burridge–Knopoff Model of Earthquakes. *Journal of the Physical Society of Japan*, *87*(5), 053001. https://doi.org/10.7566/JPSJ.87.053001

Lin, A., & Nishiwaki, T. (2019). Repeated seismic slipping events recorded in a fault gouge zone: Evidence from the Nojima fault drill holes, SW Japan. *Geophysical Research Letters*, *46*(3), 1276-1283. https://doi.org/10.1029/2019GL081927

Linker, M. F., & Dieterich, J. H. (1992). Effects of variable normal stress on rock friction: Observations and constitutive equations. *Journal of Geophysical Research: Solid Earth*, *97*(B4), 4923-4940. https://doi.org/10.1029/92JB00017

Liu, Y. (2013). Numerical simulations on megathrust rupture stabilized under strong dilatancy strengthening in slow slip region. *Geophysical Research Letters*, *40*(7), 1311-1316. https://doi.org/10.1002/grl.50298

Liu, Y., & Rice, J. R. (2005). Aseismic slip transients emerge spontaneously in three-dimensional rate and state modeling of subduction earthquake sequences. *Journal of Geophysical Research: Solid Earth*, *110*(B8). https://doi.org/10.1029/2004JB003424

Lockner, D. A., & Beeler, N. M. (1999). Premonitory slip and tidal triggering of earthquakes. *Journal of Geophysical Research: Solid Earth*, *104*(B9), 20133-20151. https://doi.org/10.1029/1999JB900205

Luo, Y., & Ampuero, J. P. (2018). Stability of faults with heterogeneous friction properties and effective normal stress. *Tectonophysics*, *733*, 257-272. https://doi.org/10.1016/j.tecto.2017.11.006

Luo, Y., & Liu, Z. (2019). Rate-and-state model casts new insight into episodic tremor and slow-slip variability in Cascadia. *Geophysical Research Letters*, *46*(12), 6352-6362. https://doi.org/10.1029/2019GL082694

Matsuzawa, T., Hirose, H., Shibazaki, B., & Obara, K. (2010). Modeling short-and long-term slow slip events in the seismic cycles of large subduction earthquakes. *Journal of Geophysical Research: Solid Earth*, *115*(B12). https://doi.org/10.1029/2010JB007566

Marone, C. (1998). Laboratory-derived friction laws and their application to seismic faulting. *Annual Review of Earth and Planetary Sciences*, *26*(1), 643-696. https://doi.org/10.1146/annurev.earth.26.1.643

Marone, C., & Kilgore, B. (1993). Scaling of the critical slip distance for seismic faulting with shear strain in fault zones. *Nature*, *362*(6421), 618-621. https://doi.org/10.1038/362618a0

Marone, C., Raleigh, C. B., & Scholz, C. H. (1990). Frictional behavior and constitutive modeling of simulated fault gouge. *Journal of Geophysical Research: Solid Earth*, *95*(B5), 7007-7025. https://doi.org/10.1029/JB095iB05p07007

Maury, J., Aochi, H., & Radiguet, M. (2014). Fault constitutive relations inferred from the 2009-2010 slow slip event in Guerrero, Mexico. *Geophysical Research Letters*, *41*(14), 4929-4936. https://doi.org/10.1002/2014GL060691

Meade, B. J., & Loveless, J. P. (2009). Predicting the geodetic signature of Mw≥ 8 slow slip events. *Geophysical Research Letters*, *36*(1). https://doi.org/10.1029/2008GL036364

Métivier, L., de Viron, O., Conrad, C. P., Renault, S., Diament, M., & Patau, G. (2009). Evidence of earthquake triggering by the solid earth tides. *Earth and Planetary Science Letters*, *278*(3-4), 370-375. https://doi.org/10.1016/j.epsl.2008.12.024

Nakata, R., Hyodo, M., & Hori, T. (2012). Numerical simulation of afterslips and slow slip events that occurred in the same area in Hyuga-nada of southwest Japan. *Geophysical Journal International*, *190*(2), 1213-1220. https://doi.org/10.1111/j.1365-246X.2012.05552.x

Nakata, R., Suda, N., & Tsuruoka, H. (2008). Nonvolcanic tremor resulting from the combined effect of Earth tides and slow slip events. *Nature Geoscience*, *1*(10), 676-678. https://doi.org/10.1038/ngeo288

Noël, C., Passelègue, F. X., Giorgetti, C., & Violay, M. (2019). Fault reactivation during fluid pressure oscillations: Transition from stable to unstable slip. *Journal of Geophysical Research: Solid Earth*, *124*(11), 10940-10953. https://doi.org/10.1029/2019JB018517

Noël, C., Pimienta, L., & Violay, M. (2019). Time‐dependent deformations of sandstone during pore fluid pressure oscillations: Implications for natural and induced seismicity. *Journal of Geophysical Research: Solid Earth*, *124*(1), 801-821. https://doi.org/10.1029/2018JB016546

Obara, K. (2002). Nonvolcanic deep tremor associated with subduction in southwest Japan. *Science*, *296*(5573), 1679-1681. https://doi.org/10.1126/science.1070378

Obara, K., Hirose, H., Yamamizu, F., & Kasahara, K. (2004). Episodic slow slip events accompanied by non-volcanic tremors in southwest Japan subduction zone. *Geophysical Research Letters*, *31*(23). https://doi.org/10.1029/2004GL020848

Peng, Y., & Rubin, A. M. (2018). Simulating Short-Term Evolution of Slow Slip Influenced by Fault Heterogeneities and Tides. *Geophysical Research Letters*, *45*(19), 10-269. https://doi.org/10.1029/2018GL078752

Perfettini, H., & Ampuero, J. P. (2008). Dynamics of a velocity strengthening fault region: Implications for slow earthquakes and postseismic slip. *Journal of Geophysical Research: Solid Earth*, *113*(B9). https://doi.org/10.1029/2007JB005398

Perfettini, H., & Schmittbuhl, J. (2001). Periodic loading on a creeping fault: Implications for tides. *Geophysical Research Letters*, *28*(3), 435-438. https://doi.org/10.1029/2000GL011686

Proctor, B., Lockner, D. A., Kilgore, B. D., Mitchell, T. M., & Beeler, N. M. (2020). Direct evidence for fluid pressure, dilatancy, and compaction affecting slip in isolated faults. *Geophysical Research Letters*, *47*(16). https://doi.org/10.1029/2019GL086767

Rice, J. R. (2006). Heating and weakening of faults during earthquake slip. *Journal of Geophysical Research: Solid Earth*, *111*(B5). https://doi.org/10.1029/2005JB004006

Rogers, G., & Dragert, H. (2003). Episodic tremor and slip on the Cascadia subduction zone: The chatter of silent slip. *Science*, *300*(5627), 1942-1943. https://doi.org/10.1126/science.1084783

Romanet, P., Bhat, H. S., Jolivet, R., & Madariaga, R. (2018). Fast and slow slip events emerge due to fault geometrical complexity. *Geophysical Research Letters*, *45*(10), 4809-4819. https://doi.org/10.1029/2018GL077579

Royer, A. A., Thomas, A. M., & Bostock, M. G. (2015). Tidal modulation and triggering of low-frequency earthquakes in northern Cascadia. *Journal of Geophysical Research: Solid Earth*, *120*(1), 384-405. https://doi.org/10.1002/2014JB011430

Rubinstein, J. L., La Rocca, M., Vidale, J. E., Creager, K. C., & Wech, A. G. (2008). Tidal modulation of nonvolcanic tremor. *Science*, *319*(5860), 186-189. https://doi.org/10.1126/science.1150558

Ruina, A. (1983). Slip instability and state variable friction laws. *Journal of Geophysical Research: Solid Earth*, *88*(B12), 10359-10370. https://doi.org/10.1029/JB088iB12p10359

Samuelson, J., Elsworth, D., & Marone, C. (2009). Shear-induced dilatancy of fluid-saturated faults: Experiment and theory. *Journal of Geophysical Research: Solid Earth*, *114*(B12). https://doi.org/10.1029/2008JB006273

Savage, H. M., & Marone, C. (2007). Effects of shear velocity oscillations on stick‐slip behavior in laboratory experiments. *Journal of Geophysical Research: Solid Earth*, *112*(B2). https://doi.org/10.1029/2005JB004238

Scholz, C. H. (1988). The critical slip distance for seismic faulting. *Nature*, *336*(6201), 761-763. https://doi.org/10.1038/336761a0

Scholz, C. H. (1998). Earthquakes and friction laws. *Nature*, *391*(6662), 37-42. https://doi.org/10.1038/34097

Scholz, C. H. (2019). *The mechanics of earthquakes and faulting*. New York, NY; Cambridge University Press. https://doi.org/10.1017/9781316681473

Scholz, C. H., Tan, Y. J., & Albino, F. (2019). The mechanism of tidal triggering of earthquakes at mid-ocean ridges. *Nature communications*, *10*(1), 1-7. https://doi.org/10.1038/s41467-019-10605-2

Schwartz, S. Y., & Rokosky, J. M. (2007). Slow slip events and seismic tremor at circum-Pacific subduction zones. *Reviews of Geophysics*, *45*(3). https://doi.org/10.1029/2006RG000208

Segall, P. (2010). *Earthquake and volcano deformation*. Princeton NJ: Princeton University Press. https://doi.org/10.1515/9781400833856

Segall, P., & Rice, J. R. (1995). Dilatancy, compaction, and slip instability of a fluid-infiltrated fault. *Journal of Geophysical Research: Solid Earth*, *100*(B11), 22155-22171. https://doi.org/10.1029/95JB02403

Segall, P., Rubin, A. M., Bradley, A. M., & Rice, J. R. (2010). Dilatant strengthening as a mechanism for slow slip events. *Journal of Geophysical Research: Solid Earth*, *115*(B12). https://doi.org/10.1029/2010JB007449

Shelly, D. R., Beroza, G. C., & Ide, S. (2007a). Non-volcanic tremor and low-frequency earthquake swarms. *Nature*, *446*(7133), 305-307. https://doi.org/10.1038/nature05666

Shelly, D. R., Beroza, G. C., & Ide, S. (2007b). Complex evolution of transient slip derived from precise tremor locations in western Shikoku, Japan. *Geochemistry, Geophysics, Geosystems*, *8*(10). https://doi.org/10.1029/2007GC001640

Shelly, D. R., Beroza, G. C., Ide, S., & Nakamula, S. (2006). Low-frequency earthquakes in Shikoku, Japan, and their relationship to episodic tremor and slip. *Nature*, *442*(7099), 188-191. https://doi.org/10.1038/nature04931

Shelly, D. R., Peng, Z., Hill, D. P., & Aiken, C. (2011). Triggered creep as a possible mechanism for delayed dynamic triggering of tremor and earthquakes. *Nature Geoscience*, *4*(6), 384-388. https://doi.org/10.1038/ngeo1141

Shibazaki, B., & Iio, Y. (2003). On the physical mechanism of silent slip events along the deeper part of the seismogenic zone. *Geophysical Research Letters*, *30*(9). https://doi.org/10.1029/2003GL017047

Shibazaki, B., Obara, K., Matsuzawa, T., & Hirose, H. (2012). Modeling of slow slip events along the deep subduction zone in the Kii Peninsula and Tokai regions, southwest Japan. *Journal of Geophysical Research: Solid Earth*, *117*(B6). https://doi.org/10.1029/2011JB009083

Suzuki, T., & Yamashita, T. (2009). Dynamic modeling of slow earthquakes based on thermoporoelastic effects and inelastic generation of pores. *Journal of Geophysical Research: Solid Earth*, *114*(B6). https://doi.org/10.1029/2008JB006042

Tan, Y. J., & Marsan, D. (2020). Connecting a broad spectrum of transient slip on the San Andreas fault. *Science advances*, *6*(33), eabb2489. https://doi.org/10.1126/sciadv.abb2489

Tanaka, S. (2012). Tidal triggering of earthquakes prior to the 2011 Tohoku‐Oki earthquake (Mw 9.1). *Geophysical research letters*, *39*(7). https://doi.org/10.1029/2012GL051179

Tanaka, S. (2010). Tidal triggering of earthquakes precursory to the recent Sumatra megathrust earthquakes of 26 December 2004 (Mw 9.0), 28 March 2005 (Mw 8.6), and 12 September 2007 (Mw 8.5). *Geophysical Research Letters*, *37*(2). https://doi.org/10.1029/2009GL041581

Thomas, A. M., Beeler, N. M., Bletery, Q., Burgmann, R., & Shelly, D. R. (2018). Using low-frequency earthquake families on the San Andreas Fault as deep creepmeters. *Journal of Geophysical Research: Solid Earth*, *123*(1), 457-475. https://doi.org/10.1002/2017JB014404

Thomas, A. M., Bürgmann, R., Shelly, D. R., Beeler, N. M., & Rudolph, M. L. (2012). Tidal triggering of low frequency earthquakes near Parkfield, California: Implications for fault mechanics within the brittle-ductile transition. *Journal of Geophysical Research: Solid Earth*, *117*(B5). https://doi.org/10.1029/2011JB009036

Thomas, A. M., Nadeau, R. M., & Bürgmann, R. (2009). Tremor-tide correlations and natthostatic pore pressure on the deep San Andreas fault. *Nature*, *462*(7276), 1048-1051. https://doi.org/10.1038/nature08654

van der Elst, N. J., Delorey, A. A., Shelly, D. R., & Johnson, P. A. (2016). Fortnightly modulation of San Andreas tremor and low-frequency earthquakes. *Proceedings of the National Academy of Sciences*, *113*(31), 8601-8605. https://doi.org/10.1073/pnas.1524316113

Vidale, J. E., Agnew, D. C., Johnston, M. J., & Oppenheimer, D. H. (1998). Absence of earthquake correlation with Earth tides: An indication of high preseismic fault stress rate. *Journal of Geophysical Research: Solid Earth*, *103*(B10), 24567-24572. https://doi.org/10.1029/98JB00594

Villafuerte, C., & Cruz-Atienza, V. M. (2017). Insights into the causal relationship between slow slip and tectonic tremor in Guerrero, Mexico. *Journal of Geophysical Research: Solid Earth*, *122*(8), 6642-6656. https://doi.org/10.1002/2017JB014037

Wein, A. S., & Shearer, P. M. (2004, December). A comprehensive search for tidal triggering of Southern California earthquakes. In *AGU Fall Meeting Abstracts* (Vol. 2004, pp. S23A-0297).

Yabe, S., Tanaka, Y., Houston, H., & Ide, S. (2015). Tidal sensitivity of tectonic tremors in Nankai and Cascadia subduction zones. *Journal of Geophysical Research: Solid Earth*, *120*(11), 7587-7605. https://doi.org/10.1002/2015JB012250

Yamashita, T., & Tsutsumi, A. (2018). *Involvement of fluids in earthquake ruptures.* Tokyo, Japan: Springer. https://doi.org/10.1007/978-4-431-56562-8

Journal of Geophysical Research: Solid Earth

Supporting Information for

Frictional and Hydraulic Properties of Plate Interfaces Constrained by a Tidal Response Model Considering Dilatancy/Compaction

Ryunosuke Sakamoto[1] and Yoshiyuki Tanaka[2]

[1]Department of Earth and Space Science, Osaka University, Osaka, Japan

[2]Department of Earth and Planetary Science, The University of Tokyo, Tokyo, Japan

Contents of this file

Text S1, S2, S3 and S4

Figures S1, S2, S3, S4, S5 S6, S7 and S8

Introduction

TextS1 presents the governing equation of the drained model.

TextS2 presents the nondimensionalized governing equation of the drained model.

TextS3 presents a numerical method for solving the governing equation of the drained model.

TextS4 presents the approximate solution for the tidal response of the drained model.

Figure S1 shows a schematic of the undrained and drained models.

Figure S2 shows the numerical solution of c in equation (12) for the undrained model.

Figure S3 shows the numerical and approximate solutions for the tidal responses α and δ of the drained model.

Figure S4 shows the numerical solution of c in equation (12) for the drained model.

Figure S5 shows the time variation of the tidal Coulomb stress term ($\Delta S(t)$ of equation (21)), the dilatancy/compaction effect term and the evolution effect term in equation (21).

Figure S6 shows a schematic illustration of the relationship between the fault creep velocity and the tide level when $U = 1$.

Figure S7 shows the dependence of the parameter E_p on the phase difference.

Figure S8 shows the dependence of d_c on the tidal sensitivity and phase difference when $V_{pl} = 10^{-7}$ and 10^{-9} $\mathrm{m/s}$.

Text S1. Derivation of the governing equations for the drained model

We explain a drained model in which pore fluids flow out of the shear zone (Figure S1b). The difference between the undrained and drained models is the presence of fluid flow. The governing equations of the drained model are the same as those in the undrained model (equations (3), (4) and (8)), except for the governing equation for pore fluids.

Following the work of Segall et al. (2010), we assume homogeneous diffusion (HD), which holds under the condition that $T \gg t_w$. In the HD case, the effect of the finite shear zone thickness can be neglected, so the width of the shear zone can be formally defined as $w \to 0$ (Segall et al., 2010). The direction of fluid flow (Figure S1b) is parallel to the z-axis, and the shear zone lies on $z = 0$. c_{hyd} denotes the fluid pressure diffusivity at $z \neq 0$. Then, the governing equation for pore fluids can be written as (Segall et al., 2010)

$$\frac{\partial p}{\partial t} = c_{hyd} \frac{\partial^2 p}{\partial z^2} \ \left(\left. \frac{\partial p}{\partial z} \right|_{z=0} = \frac{Mw\dot{\phi}}{2c_{hyd}} \right). \tag{S1}$$

Text S2. Nondimensionalization of the governing equations of the drained model

The governing equations for the drained model are the upper three in equation (10) and the nondimensionalized equation (S1). When we adopt $\sqrt{c_{hyd}T}$ as the representative length in the z-axis direction, the nondimensionalized equation (S1) can be written as

$$\frac{\partial \tilde{p}}{\partial \tilde{t}} = \frac{\partial^2 \tilde{p}}{\partial \tilde{z}^2} \ \left(\left. \frac{\partial \tilde{p}}{\partial \tilde{z}} \right|_{\tilde{z}=0} = -E_p \frac{1}{\tilde{\theta}} \frac{d\tilde{\theta}}{d\tilde{t}} \right), \tag{S2}$$

where $E_p = M\epsilon/2\sigma_{eff}^0 \sqrt{w^2/Tc_{hyd}} = U/2\sqrt{w^2/Tc_{hyd}}$. E_p represents the relative importance of the dilatancy/compaction effect to the effective normal stress change in the drained model. Previous experiments and observations suggest that $c_{hyd} \sim 10^{-1\sim 3}$ $\mathrm{m^2/s}$ (Yamashita and Tsutsumi, 2018) and $U \sim 10^{0\sim -2}$ (Section 2.2.3). Using $10^{0\sim 1/2}$ m as the value of w (Section 4.3.4), we obtain a possible range of E_p as 10^{-2} to 10^{-4}.

Text S3. A numerical method for solving the governing equation of the drained model

The upper three equations in equation (10) are calculated numerically using the third-order Adams-Bashforth method as in the undrained case. Equation (S2) is calculated numerically using the method presented in Appendix B of Segall et al. (2010). In the following, we discuss the latter method. Near the shear zone, the discretization needs to be sufficiently fine to capture a steep gradient of the pore fluid pressure. On the other hand, for a region far from the shear zone, the discretization does not need to be fine because the pore fluid pressure gradient is small. Thus, we use the following coordinate transformation between z and r (Segall et al., 2010):

$$z(r) = -c + e^{\mathrm{r}} \text{ or, equivalently, } r(z) = \ln(c + z).$$

We solve equation (S2) numerically in a new coordinate system using the Crank-Nicolson method. Specifically, we solve

$$\begin{aligned} &\left\{1 + \frac{\gamma}{2} e^{-r_k}\left(e^{-(r_k-\delta)} + e^{-(r_k+\delta)}\right)\right\} p_k^{i+1} \\ &= p_k^i + \frac{\gamma}{2} e^{-r_k} e^{-(r_k-\delta)}\left(p_{k-1}^i + p_{k-1}^{i+1}\right) - \frac{\gamma}{2} e^{-r_k} p_k^i\left(e^{-(r_k-\delta)} + e^{-(r_k+\delta)}\right), \end{aligned} \tag{S3}$$

where $\gamma = \Delta t/\Delta r^2$, $\delta = \Delta r/2$, and p_i^k is the value of the pore fluid pressure of the k-th grid in the new coordinate system at time step i. Δt andΔr represent increments in time and space, respectively. In this study, the number of grids is 35, and the starting position of the grid is $r(0) = \ln(0)$, $\Delta r = 0.3$, and $c = 10^{-4}$. Therefore, the grid farthest from the shear zone in the numerical calculation using $c_{hyd}{\sim}10^{-1}\ \mathrm{m^2/s}$, $T{\sim}12.4$ h is approximately $z = 170$ m, while the grid farthest from the shear zone in the numerical calculation using $c_{hyd}{\sim}10^{-3}\ \mathrm{m^2/s}$, $T{\sim}12.4$ h is approximately $z = 17$ m.

Text S4. The approximate solution for the tidal response of the drained model

The approximate solution for the drained model is derived in the same manner as in Section 3.1. The pore fluid pressure change due to fluid flow is represented as $p(z,t) = p_0 + \Delta p(z)e^{i\omega t}$, where $p(0,t)$ corresponds to the pore fluid pressure in the shear zone. The equations for the drained model corresponding to equations (13) and (14) for the undrained model are

$$\frac{\Delta\tilde{V}}{\tilde{V}_{pl}} = \frac{2\pi i}{\tilde{K}\tilde{V}_{pl} + 2\pi iC}|\Delta\tilde{S}(t)| \tag{S4}$$

and

$$C = a - \frac{1}{1 + i\frac{T_\theta}{T}}\left(b - \mu_{pl}E_p\sqrt{2\pi i}\right), \text{respectively.} \tag{S5}$$

The equations of the drained model corresponding to equations (17) and (18) for the undrained model are

$$\alpha = Re\left(\frac{2\pi i}{(\tilde{K}\tilde{V}_{pl} + 2\pi iC)\sigma_{eff}^0}\right) \tag{S6}$$

and

$$\delta = arg\left(\frac{2\pi i}{\tilde{K}\tilde{V}_{pl} + 2\pi iC}\right), \text{respectively.} \tag{S7}$$

Furthermore, by applying the argument from which equations (19) and (20) were derived for the drained model, the approximate solutions of α and δ can be expressed as

$$\alpha \sim Re\left\{\left(C\sigma_{eff}^0\right)^{-1}\right\} \tag{S8}$$

and

$$\delta \sim arg\{C^{-1}\}, \tag{S9}$$

respectively.

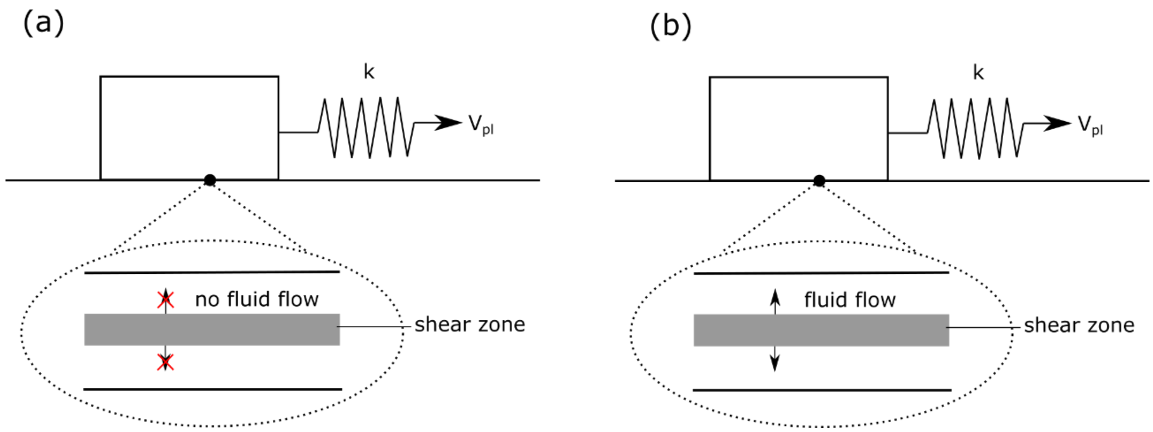

Figure S1. A schematic of the undrained (a) and drained (b) models. The difference between the two models is whether fluid flows outside the shear zone**.**

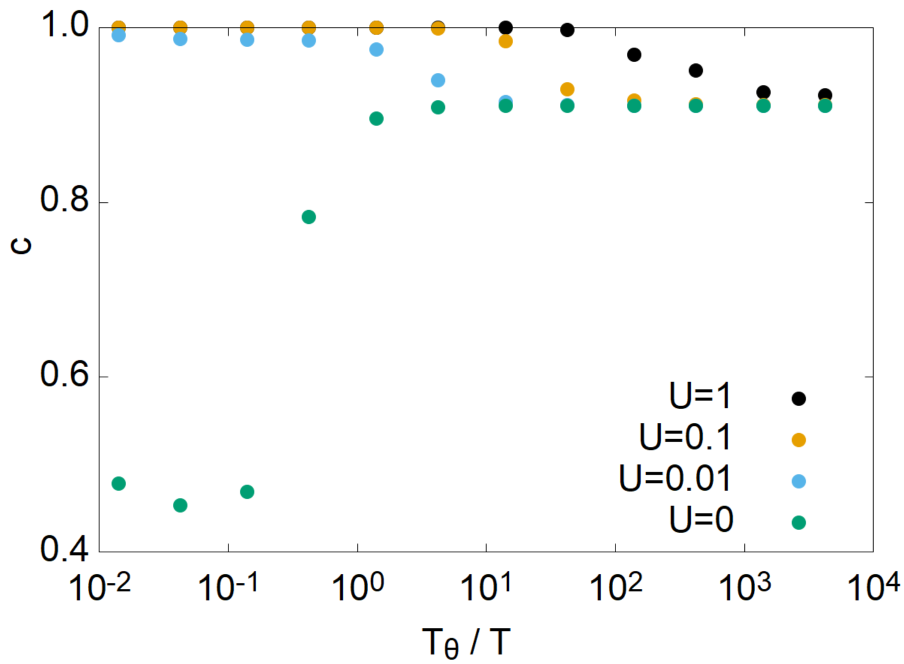

Figure S2. The numerical solution of $\boldsymbol{c}$ (dots). The differences in color represent differences in the dilatancy parameter $\boldsymbol{U}$.

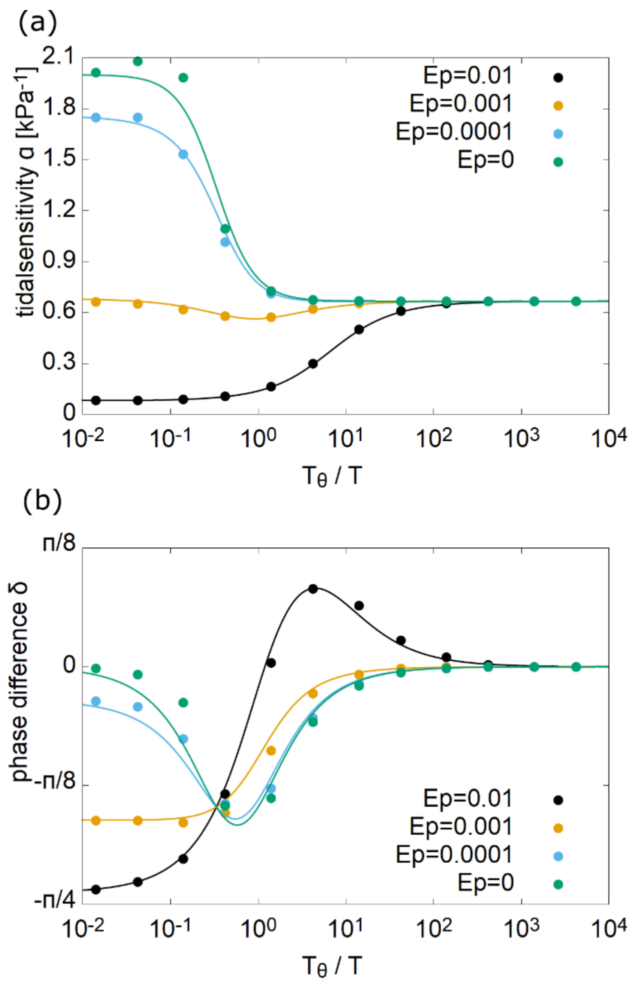

Figure S3. (a) The numerical solution of $\boldsymbol{\alpha}$ (dots) and the approximation solution (i.e., equation (S8)) (solid line). (b) The numerical solution of $\boldsymbol{\delta}$ (dots) and the approximation solution (i.e., equation (S9)) (solid line). The differences in color represent differences in the dilatancy parameter $\boldsymbol{E_p}$ for the drained model.

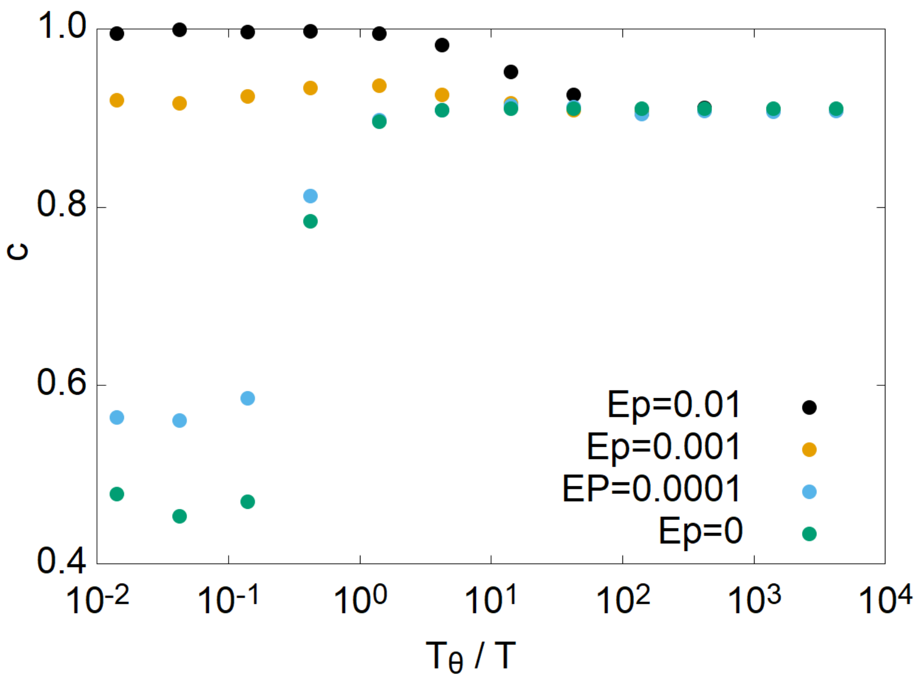

Figure S4. The numerical solution of $\boldsymbol{c}$ (dots). The differences in color represent differences in the dilatancy parameter $\boldsymbol{E_p}$ for the drained model.

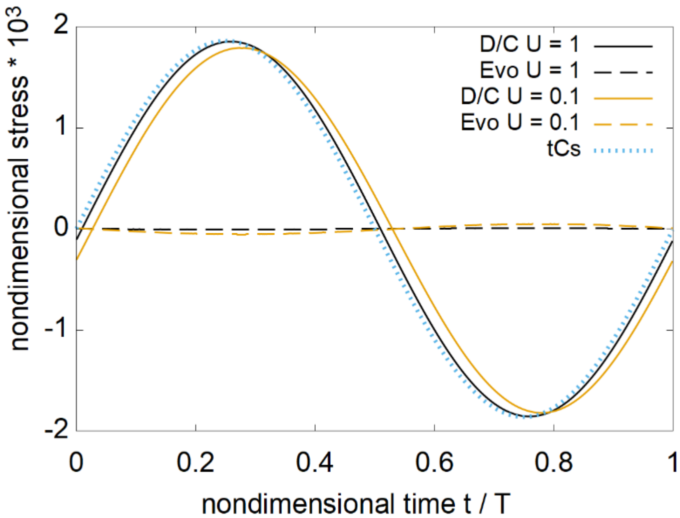

Figure S5. The time evolution of the dilatancy/compaction (D/C) term and the evolution (Evo) term for $U = 1$ and $U = 0.1$ (the variation from the time average over one tidal cycle is shown). The horizontal axis denotes the time normalized by the tidal period, and the values from 0 to 1 indicate one tidal cycle. The vertical axis denotes the tidal Coulomb stress (tCs) $\times\, 10^3$, normalized by the frictional strength σ_{eff}^0. The numerical solutions for $T_\theta/T = 14$ and $U = 1$ are shown in black, and those for $T_\theta/T = 4.2$ and $U = 0.1$ are shown in yellow. The amplitudes of the D/C term and tCs term are almost the same for $U = 0.1$ as well as $U = 1$. This means that the argument in Lines 407-414 in the body text can be applied to $U = 0.1$ as well as $U = 1$. Furthermore, the D/C term for $U = 0.1$ has a phase shift to the right of that for $U = 0.1$. Thus, $\beta(\ll \pi)$ at $U = 0.1$ is larger than $\beta(\ll \pi)$ at $U = 1$ ($\log\left(V/V_{pl}\right) \sim |\Delta S(t)| \sin(\beta/2) \cos(\omega t + (\pi - \beta)/2)$. See Appendix B). Since the tidal Coulomb stress peak corresponds to $\omega = \pi/2$, the larger β is, the smaller δ is. In other words, δ is smaller for $U = 0.1$ than for $U = 1$.

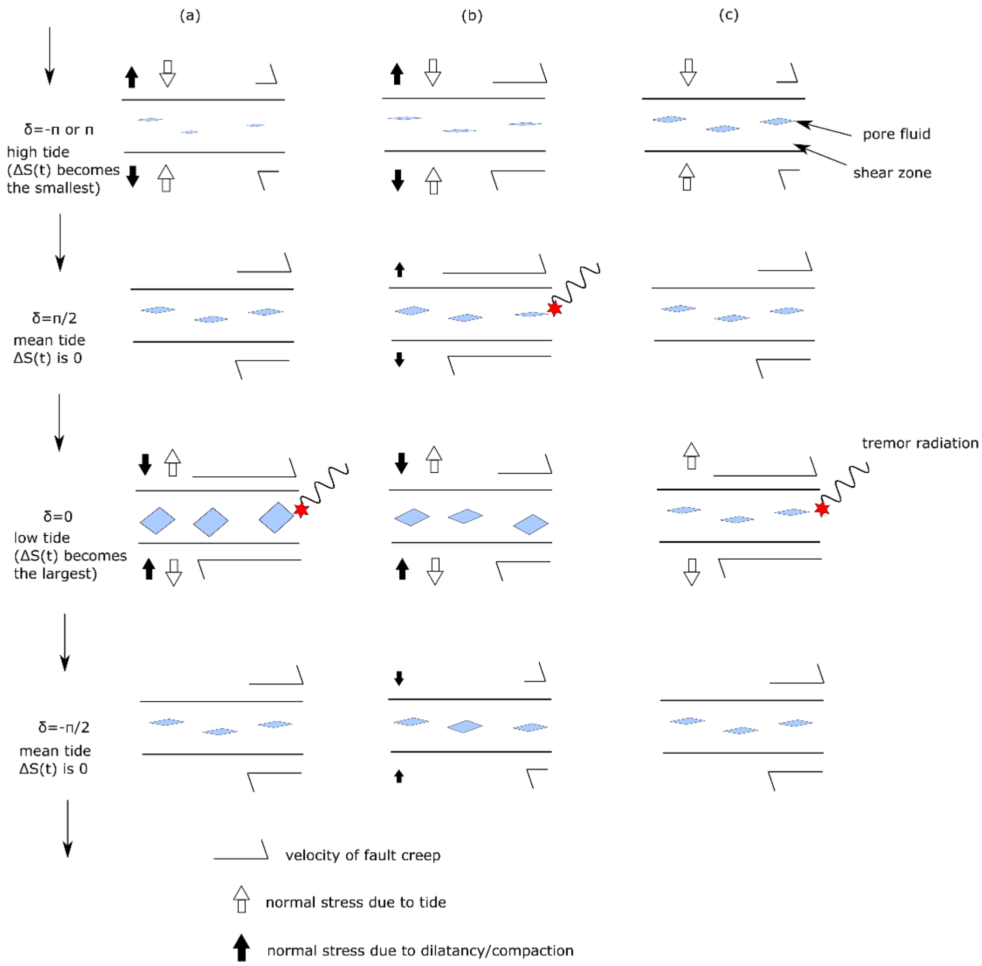

Figure S6. A schematic illustration of the relationship between the fault creep velocity and tide level when $U = 1$. For simplicity, only the normal stress change (white arrows) is represented. (a) Tidal modulation of fault creep when $T_\theta/T \ll 1$. Since the dilatancy/compaction effect (black arrows) decreases the amplitude of $\Delta S(t)$, the fault creep velocity reaches its maximum at $\delta \sim 0$. (b) Tidal modulation of fault creep when $T_\theta/T \ll 1$ and $T_\theta/T \gg |b - \mu_{pl}U|/a$. The sum of the normal stress due to the dilatancy/compaction effect and the tidal normal stress becomes the largest in the sense of enhancing fault slip at $\delta \sim \pi/2$. (c) Tidal modulation of fault creep when $T_\theta/T \gg |b - \mu_{pl}U|/a$. The dilatancy/compaction effect is negligible, and the fault creep velocity reaches its maximum at $\delta \sim 0$.

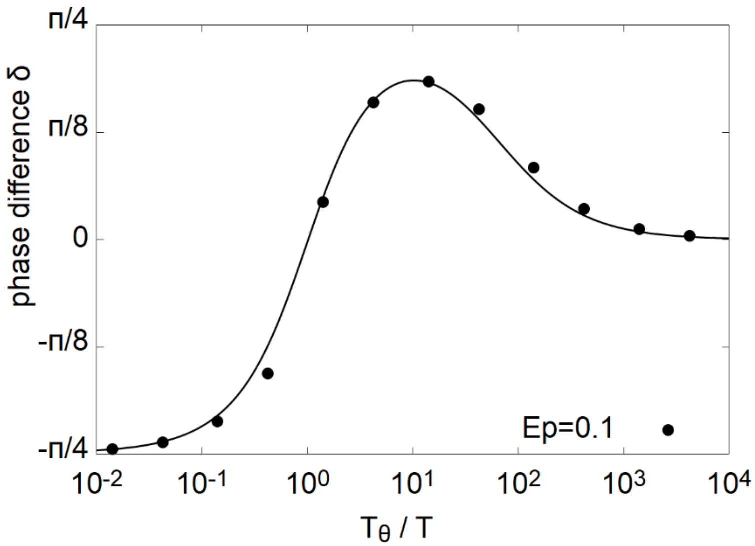

Figure S7. The dependence of T_θ/T on the phase difference at $E_p = 0.1$ The numerical solution of δ (dots) and the approximation solution (i.e., equation (S9)) (solid line). We see that the maximum phase difference is $\delta \sim \pi/6$ at $T_\theta/T \sim 10$, which cannot explain the observed phase difference of $\pi/2$.

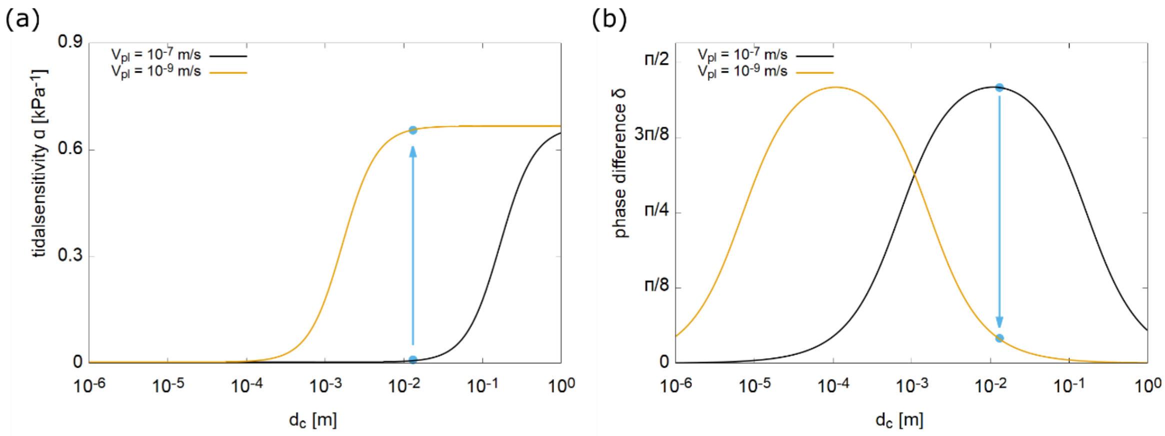

Figure S8. (a) The approximation solution of α (equation (19)) when $V_{pl} = 10^{-7}$ m/s (black) and 10^{-9} m/s (yellow). The horizontal axis denotes the critical slip distance d_c. The blue dots show that α for $d_c = 0.13$ m increases from $\lesssim 0.1$ to ~ 0.7 as V_{pl} decreases from 10^{-7} m/s to 10^{-9} m/s. (b) The same as in (a) but for the approximation solution of δ (equation (20)). The blue dots show that δ decreases from $\sim \pi/2$ to ~ 0 as V_{pl} decreases from 10^{-7} m/s to 10^{-9} m/s.